Numerical Simulation of Momentum Transport Processes through Gas-Liquid Interface

Yousuke Abe

DOCTOR OF *SCIENCE*

Department of Fusion Science

School of Physical Sciences

The Graduate University for Advanced Studies

2005 (School Year)

Abstract

Free-surface turbulent flows are ubiquitously found in the nature as well as in various industrial devices such as a chemical plant, not to mention the turbulence in rivers and oceans. A two-phase flow for a gas and a liquid with a distorted interface is one of the most common issues for free-surface turbulent flows, and, recently, has been much paid attention to in the field of environmental science, specifically, in the climate projection study. Interaction between Atmosphere and Ocean is a key issue in the climate projection because their interaction affects the global circulation as well as the local weather. At the Earth Simulator Center, a high-resolution (100m - 10km for horizontal) non-hydrodynamic Atmosphere-Ocean coupling model has been developed in order to simulate not only a global phenomenon, but also a local one, such as a typhoon which may bring a terrible disaster. In this high-resolution regime, however, no reliable method of evaluating physical quantities, such as the momentum, heat, and vapor, exchanged through the interface has been established. Therefore, it is necessary to investigate fundamental physical processes in gas-liquid flows with a free-surface.

In previous studies on the gas-liquid flows with a free-surface, mainly explored was the liquid side turbulence near the interface on which no or very low shear flow condition was imposed. A direct numerical simulation (DNS) of free-surface flows with the coupled gas-liquid dynamics should be useful for understanding a gas-liquid interaction mechanism through a detailed analysis of turbulent statistics which can not be obtained by experiments. Nevertheless, only a few trials have been made because of the numerical difficulties in tracking a free-surface, such as the numerical diffusion and instability accompanied with the interface deformation. Since, in a high velocity range commonly seen in realistic free-surface flows, turbulent characteristics near a free-surface could be influenced by deformation of the free-surface due to wind shear, it is necessary to take into account the effects of the interface distortion in the DNS of the gas-liquid flow simulation.

Various kinds of two-phase flow models have been developed such as the level-set method and the volume-of-fluid (VOF) method. Recently, Kunugi (1997) has developed a precise free-surface tracking algorithm for two-phase flows, that is, Multi-interfaces Advection and Reconstruction Solver (MARS). Yabe and Wang (1991) proposed the CIP-combined, unified procedure (C-CUP method) which can treat the compressible and incompressible fluids, simultaneously, in the same code. Even in cases that an interface is largely deformed by a strong wind shear, the C-CUP method can resolve the complicated interfaces on the Cartesian coordinates. Since it is not necessary to reconstruct the numerical grid in the C-CUP method, the numerical cost and errors can be reduced in comparison to MARS. Using the C-CUP method, Mutsuda et al. (1998, 1999) succeeded in performing a DNS of wave-breaking and entrained air bubble in a gas-liquid

turbulent layer. However, there has been no quantitative evaluation of the friction stress by means of the two-phase flow simulation.

The objective of this study is to show the validity of the numerical method based on the C-CUP scheme, by quantitatively comparing the simulation results with experimental data, towards construction of a reliable method for evaluating the friction stress between Atmosphere and Ocean. The reasons for adopting the C-CUP method are summarized as follows. First, applicability of the C-CUP method to the compressible fluid has an advantage in simulation of severe phenomena such as a typhoon. Second, the C-CUP method can keep thickness of a transition region near the sea-surface compact, which is important in long-term integration. Moreover, it is a more direct way to solve the same equations for both Atmosphere and Ocean, as is done in the C-CUP method, than separately treating them through boundary conditions on the sea-surface.

In this study, the two-phase flow simulations for a gas and a liquid are performed with a numerical setting as given bellow. Setting of the numerical domain is relevant to tank-experiments. Turbulent Reynolds number Re_τ is changed from 150 to 300 in order to find the wind velocity dependence of the friction. An effect of the water depth on evaluation of the friction velocity is also studied. In the deeper case, the water depth is relevant to that of the tank-experiments. The wind velocity is in a regime that the free-surface deformation accompanied with ripples can not be ignored, and is comparable to the representative velocity range in the tank-experiments. The continuum surface force (CSF) model, which is often used in two-phase flow simulations, proposed by Brackbill et al. (1992) is applied to the surface tension. In a transition region near the free-surface, the viscous coefficient is modeled by an inversely proportional relation which shows a better property than the linear relation and agrees with experimental data for two-phase mixing fluids by McAdams et al. (1942). In addition to the C-CUP method, the present simulation code is implemented with the following schemes in order to improve the numerical stability and accuracy in the high velocity range. The rational CIP method proposed by Xiao et al. (1996) can avoid negative values of the density and pressure in the transition region near the free-surface. The tangent transformed density function, which defines the transition region, proposed by Yabe and Xiao (1993) can reduce the numerical diffusion of the transition region keeping the compactness.

From the statistical analysis of turbulence in the simulation results, we have quantitatively discussed the turbulent structures near the free-surface and the mechanism of the momentum transfer through the gas-liquid interface. The results obtained from the present simulation study on the two-phase flow, are summarized below.

It is shown that the vertical velocity fluctuations normal to the free-surface are induced on the liquid side near the interface. To explain this behavior, we have made analysis of the pressure-strain correlation term that remains finite only near the free-surface on the liquid side. The surface-normal component of the pressure-strain correlation term has a positive value while the streamwise

component is negative. This behavior indicates that the turbulent energy on the gas side is redistributed mainly into the vertical component of the velocity fluctuations on the liquid side through the free-surface deformations which are excited by the shear stress. Moreover, the result that all vorticity components increase near the free-surface shows the presence of three-dimensional turbulent structures. Thus, it is necessary to take into account the effects of the free-surface deformation on the momentum transfer process through the gas-liquid interface when a large shear stress exists. It is also suggested that the vertical velocity component should be accurately calculated, although the conventional numerical simulations have treated the velocity fields near the free-surface as almost two-dimensional.

The turbulent structures are similar to those of the experiment, in which the representative wind velocity is almost the same as that of the present study. The Reynolds stress distribution is correlated with the free-surface structure. This result reflects that the momentum transfer through the gas-liquid interface is related to the Reynolds stress produced by the vertical velocity fluctuations near the free-surface. In order to verify the correlation, we have investigated a phase relation between a time series of the Reynolds stress on the gas side and that of the free-surface position. According to this analysis, large positive spikes of the Reynolds stress, which enhance the downward momentum transfer, often appear at positions where the 'burst' and the 'sweep' are observed. It is also consistent with the experiments. In addition, bursts of the Reynolds stress are observed in close to the crest over the windward side, as reported in the experiment. This agreement suggests that the present simulation captures the bursting phenomena produced by the Reynolds stress in relation to ordered motions such as the wind flow separation and the reattachment over wind waves. Therefore, it is considered that the momentum transfer process with the free-surface deformation can be well reproduced by the present DNS of the two-phase flow.

The friction velocities are evaluated from the peak values of the friction stresses near the free-surface on the liquid side. The relation between the friction velocity and the mean velocity on the gas side is in good agreement with the tank-experimental data for both cases of the Reynolds numbers of 150 and 300. Especially, a better agreement is found for the deeper water condition. In the velocity range considered here, the free-surface deformation can not be ignored in contrast to the conditions for the conventional DNS studies, where the liquid turbulence is decoupled from the gas dynamics by supposing a flat interface and applying the free-slip condition. Therefore, the present study presents the first quantitative evaluation of the friction stresses on the free-surface, which is validated by a comparison with the tank experimental data.

The three-second power law and the spectrum form of wind waves proposed by Toba (1972) are also examined for the case of the present numerical simulation. The form of the energy spectrum of wind waves is derived from a combination of the three-second power law and the similarity of the spectral form of wind waves. These are well substantiated by data from a wind-wave tunnel

experiment. The three-second power law is obtained from the spectrum of wind waves based on the local balance between the wind waves and both the turbulent structures of the air and liquid flows. The period and the wave height of significant waves in dimensionless forms, which are considered to correspond to the peak frequency and the energy level, respectively, are used as representative quantities of wind waves. From the results of the present study, it is confirmed that the relation of the period and the height of significant waves is consistent to the three-second power law within the error coming from the wind-wave tunnel experiment and the field observation. In the gravity wave range, the spectral form on the high frequency side is proportional to the -4 power of the angular frequency of wind waves. The wind waves grow in a way that on the logarithmic diagram of the spectral density versus the angular frequency, the spectrum slides up along the line of the form, keeping its similar form. It is confirmed that the spectral density obtained by the present simulations has the -4 power of the angular frequency. The spectrum level shows a better agreement with the data of the wind-wave tunnel experiment than that of the field observation. The result suggests that the present numerical simulation can accurately represent the developing phase of wind waves in wind-wave tunnel experiments. As the wave number becomes large, the effect of surface tension is incorporated. Thus, the -4 power line found in the gravity wave range gradually approaches the -8/3 power line for the capillary wave range, which is also reproduced by the present simulations.

The obtained results confirm that the present simulation method has a possibility of extension to a larger gas-liquid flow system towards construction of a reliable scheme for evaluating the friction stress between Atmosphere and Ocean.

Contents

1 Introduction

1.1 Background

Free-surface turbulent flows are ubiquitously found in the nature not to mention the turbulence in rivers and oceans, as well as in various industrial devices such as a chemical plant. A two-phase flow for a gas and a liquid with a distorted interface is one of the most common issues for free-surface turbulent flows, and, recently, has been much paid attention to in the field of environmental science, such as the climate projection study. Specifically, interaction between Atmosphere and Ocean is critical to the climate projection because their interaction affects the global circulation as well as the local weather prediction.

In the Earth Simulator Center, a high-resolution (100m - 10km in horizontal) non-hydrostatic Atmosphere-Ocean coupling model has been developed in order to simulate not only a global phenomenon, but also a local one, such as a typhoon which may bring a terrible disaster. However, no reliable method of evaluating physical quantities exchanged through the interface, such as the momentum, heat, and vapor, has been established in this high-resolution regime. These physical quantities exchanged between Atmosphere and Ocean have been evaluated by using empirical formulas derived from a wind velocity and stability of Atmosphere at a reference height. In a high-resolution regime, however, it is considered that effects of the wind-waves and the wave-swellings on evaluation of the exchanged physical quantities can not be ignored. Moreover, it is difficult to verify the conventional formula because of difficulties in direct observations in the high wind regions such as a typhoon. Therefore, it is necessary to investigate fundamental physical processes in gas-liquid flows with a free-surface.

1.2 Problems in Bulk Method

1.2.1 What Is the Bulk Method?

In order to understand the necessity for investigating fundamental physical processes in gas-liquid flows with a free-surface, problems in the so-called bulk method are summarized below. The bulk method is a conventional and empirical model which is employed for evaluating of the physical quantities exchanged between Atmosphere and Ocean.

With development of computer devices, global simulation models for the Atmosphere and Ocean and their coupling have been developed as a tool for the climate projection. The global simulations need a model for the boundary conditions on the sea-surface, through which motions of Atmosphere and Ocean are determined. Also, in the coupling model of Atmosphere and Ocean, the exchanged fluxes of the momentum, the heat, and the vapor on the sea-surface should be verified by

the observations, since they are critical to determination of strength of the interaction between Atmosphere and Ocean.

The bulk method has been used for evaluating of the momentum flux, sensible heat flux, and latent heat flux, in terms of some quantities averaged over some time at a surface and at a certain height. These fluxes are calculated as

$$\tau_x = \rho C_D |\mathbf{V}| u \quad : \quad \text{The momentum flux for east-west component} \tag{1.1}$$

$$\tau_y = \rho C_D |\mathbf{V}| v \quad : \quad \text{The momentum flux for north-south component} \tag{1.2}$$

$$Q_H = \rho C_P C_H |\mathbf{V}| (T_s - T_a) \quad : \quad \text{The sensible heat flux} \tag{1.3}$$

$$Q_E = \rho L C_E |\mathbf{V}| (q_s - q_a) \quad : \quad \text{The latent heat flux} \tag{1.4}$$

where ρ, C_P, and L represent the air density, the specific heat at constant pressure, and the latent heat for evaporation, respectively. The absolute wind velocity and its east-west and north-south components, are denoted by $|\mathbf{V}|$, u and v, respectively. Also, T_a, q_a, T_s and q_s mean the air temperature, the specific humidity, the sea-surface temperature, and the saturated specific humidity in the air at the same temperature for the sea-surface, respectively. Generally, values of the quantities in the air at 10m height from the sea-surface are employed in Eq. (1.1) – (1.4). The sea-surface temperature is defined by a bulk sea temperature averaged from the surface to about 10cm depth. Non-dimensional numbers, C_D, C_H, and C_E are called the exchanging (or bulk) coefficients for the momentum, sensible heat, and latent heat, respectively. These coefficients are functions of the wind velocity and stability. The stability is also a function of the wind velocity and the temperature difference between the sea-surface and the air. The proposed bulk coefficients are parameterized using the data averaged over about 10min, because the energy spectra have their peaks at periods less than several minutes which no significant peak observed from 10min to some hours in the Atmospheric boundary layer.

As mentioned above, it is possible to estimate all of the fluxes if one observes the wind velocity, the wind direction, the air temperature, the sea-surface temperature, and the relative humidity or dew point temperature in the frame of the bulk method. It should be noted that most of the researchers in the field of the global circulation use the same equations as Eq. (1.1) – (1.4) to estimate the fluxes, but dependence of the bulk coefficients on the wind velocity and stability are different among the researchers. Therefore, it is an unresolved problem what kind of the bulk coefficients should be used for the estimation of the sea-surface fluxes.

1.2.2 Uncertainties of Bulk Coefficients and Empirical Formulations

The annual mean heat flux in the East Pacific equatorial region, the so-called warm pool, has been noticed as the area where the El Nino/ southern oscillation phenomena occur. However,

different values of the heat flux from 20 to 100Wm^{-2} are evaluated by each researcher. If the 80Wm^{-2} in the heat flux is converted into the water temperature change for 100m height of the water column, the difference could bring about $6C°$ per one year. It is not necessary to say that the difference exceeds the permissible range. On the other hand, Bunker et al. [1] compared the heat transportation estimated from the observations with that calculated from a climate model with the bulk method, and showed that the difference between the two cases reached almost one order. They concluded that, even if the bulk method has enough accuracy, the sea-surface flux includes an error, since the reported data from the ships should have bias. In this circumstance, Bryden [2] pointed out that, the estimation of the medional heat transport using the sea-surface flux is doubtful. As mentioned above, there are differences between researchers for the flux estimation. Time variation of the stored heat is also inconsistent with other data. It is, therefore, uncertain how reliable the estimated fluxes are.

Figure 1.1 shows, the dependence of the bulk coefficients for the momentum and sensible heat on the wind velocity mainly used in the conventional studies [3]. There are about 30% differences among the researchers for coefficients C_D and C_H. The bulk method is used to parameterize the turbulent transport in the lower Atmospheric boundary layer by means of a few averaged values. The problem is whether the empirical methods give sufficiently accurate estimations of the fluxes under many different conditions, since the coefficients should involve the uncertainties under the different sea conditions and their seasonal variations.

On the other hand, it has been pointed out that the friction coefficient, which depends on the wind velocity and the stability, can not be parameterized accurately without information on the wind waves at the sea-surface. Toba and Koga [4] have shown that C_D strongly depends on the wave age (a ratio of a phase speed of a wind wave to a friction velocity). Moreover, Toba et al. [5] proposed a model of the friction coefficients as shown in Fig. 1.2 by verifying the sampled data more accurately under different wave age conditions. According to their results, the friction coefficient for a high wind velocity (such as U_{10}～20m/s) is about three times larger than the estimated value as shown in Fig. 1.1, when the periodicity of the wind wave is 10s.

From a different view point, it is difficult to accurately parameterize the bulk coefficients under a very high wind velocity regime such as a typhoon [6]. This is because only a few direct observations have been made under the very high wind velocity. Thus, the accuracy of the bulk coefficients under the wind velocity higher more than about 20m/s is doubtful.

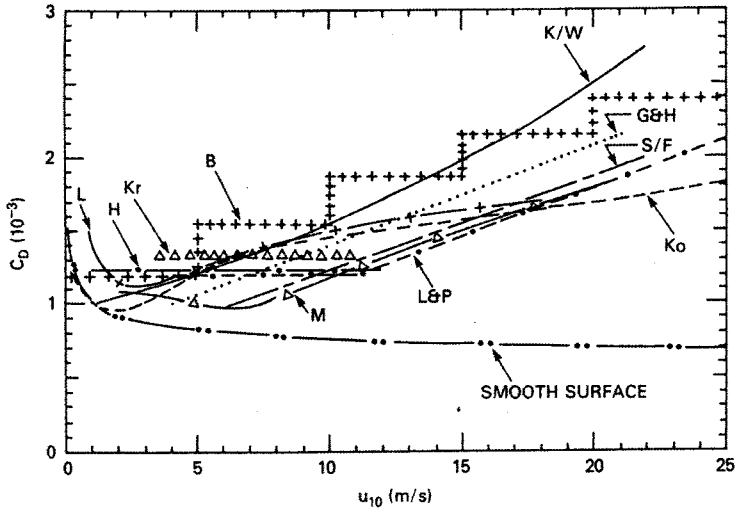

(a) Drag coefficients (C_D) for the ten selected schemes and for a smooth surface under neutral or slightly unstable conditions as a function of the wind speed at an altitude of 10m.

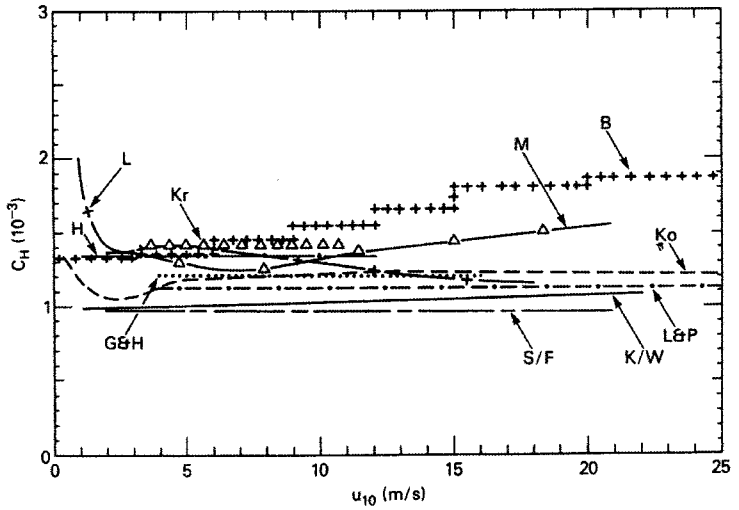

(b) Sensible heat coefficients (C_H) for the ten selected schemes under neutral or slightly unstable conditions as a function of the wind speed at an altitude of 10m.

Fig. 1.1: Dependence of the bulk coefficients on the wind velocity mainly used in the previous study [3].

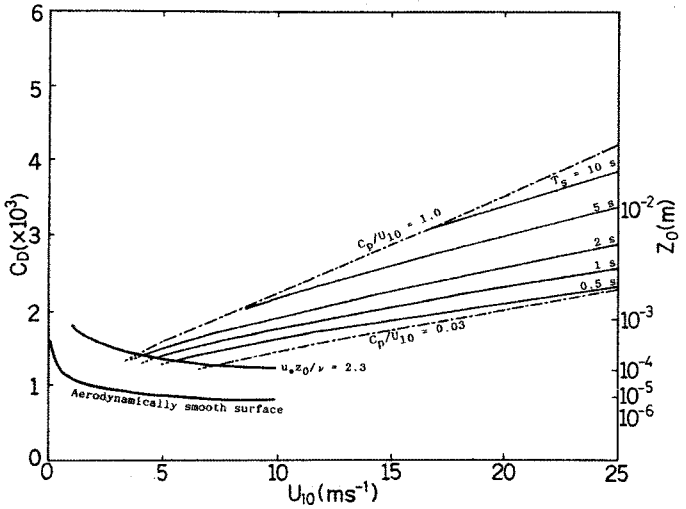

Fig. 1.2: Diagram for the drag coefficient for a neutral stability atmosphere, as a function of the wind speed at an altitude of 10m and the significant wave period [5].

1.3 Previous Studies

1.3.1 Open-Channel Turbulent Flows

In previous studies on the gas-liquid flows with a free-surface, mainly explored was the liquid side turbulence near the interface on which no or very low shear flow condition was imposed [7-12]. In experimental investigations, Komori et al. [7] extensively measured turbulent characteristics near the free-surface, and showed that, if the free-surface deformation can be ignored, the streamwise and spanwise turbulent intensities increased on liquid side while constraining vertical motions. Rashidi and Barnerjee [8] investigated large coherent structures near the free-surface, and reported that the burst motions caused typical rolling structures which enhanced the turbulent transport on the liquid side. Although the experimental investigations with superimposed wind stress have been less extensive because of difficulties in measuring the free-surface deformation caused by the wind-waves, similar phenomena to those found in the wall turbulence have been identified, such as the formation of streaks and bursts on the liquid side at high enough shear rates [13-15].

1.3.2 DNS for Open-Channel Turbulent Flows

A direct numerical simulation (DNS) of free-surface flows with the coupled gas-liquid dynamics should be useful for understanding a gas-liquid interaction mechanism. The numerical analysis of the detailed turbulent statistics provides us valuable information which can not be obtained by experiments.

Lam and Barnerjee [16] performed a 3-dimensional DNS for a liquid turbulence where the

liquid motion is decoupled from the gas dynamics by applying a mean shear boundary condition on a flat free-surface. They have confirmed that the shear rate is more important than the type of the boundary conditions in determining the dominant flow structure on the liquid side. This result agrees with the experimental evidence found by Rashidi and Barnerjee [13] under almost the same conditions. Handler et al. [17] performed a DNS of a flow confined in a region between a non-slip wall and a shear free boundary, and showed that the vertical component of turbulent energy near at the free-surface is mainly transformed into the spanwise one by the pressure-strain term. The DNS with a coupled motion of a gas and a liquid was performed by Lombardi et al. [18] by applying continuity conditions for the velocities and shear stresses at the free-surface. They have compared the results with the experiment by Rashidi and Barnerjee [13], although a flat interface is assumed to be maintained in their simulations.

As of today, only a few trials of DNS of tracking a free-surface motion have been made because of the numerical diffusion and instability accompanied with the interface deformation. In a high velocity range commonly seen in realistic free-surface flows, turbulent characteristics near a free-surface could be influenced by deformation of the free-surface due to wind shear. Moreover, it is known that the transfer process of the physical quantities are results of nonlinear interactions of wind-waves, shear stresses, and turbulent structures, on liquid side [19]. Therefore, it is necessary to take into account the effects of the interface distortion in the DNS of the gas-liquid flow simulation.

1.3.3 Two-Phase Flow Simulations in A Gas-Liquid System

In simulations of the deformable free-surface flow, it is difficult to define the positions of a free-surface, because the numerical diffusion degrades accuracy of the solution of the advection equation which describes a temporal variation of a scalar with a steep gradient at the interface. Treatment of the interface that lies between materials of different properties remains a formidable challenge in computation of multiphase fluid dynamics. Generally, Eulerian methods use color function to distinguish regions containing different materials and is robust in simulating flows with interfaces of complex topologies. In order to accurately reproduce the physical processes in a transition region near the free surface, it is quite important to maintain compactness of the interface. The finite-difference schemes constructed on Eulerian grids, however, intrinsically lead to the numerical diffusions. Thus, the direct implementation of finite-difference schemes, even with high order accuracy, cannot help to maintain the compactness of the interface.

Various kinds of numerical method of a two-phase flow have been developed to correctly simulate a compact interface. The widely used algorithms are the level-set method and the volume-of-fluid (VOF) method for front capturing or tracking [20]. The level-set method proposed by Osher et al. [21-23] avoids computing interfacial discontinuity by evaluating the field in higher dimensions. The interface of interest is then recovered by taking a subset of the field, and is,

practically defined by the zero-level set of a distance function from the interface. In the VOF methods, on the other hand, the interface needs to be reconstructed based on the volume fraction of fluid. The VOF methods are mainly classified as SLIC (simple line interface calculation) algorithms or PLIC (piecewise linear interface calculation) algorithms according to the interpolation function used for representation of the interfaces. The SLIC [24] algorithm makes use of the piecewise constant reconstruction, where the interfaces are approximated by lines aligned with mesh coordinates. A significant improvement in the VOF method was made by Youngs by means of the PLIC algorithm [25]. Then, several improvements in the reconstruction methods have been reported [26-28]. In the PLIC algorithm, the interface position is estimated by use of a truly piecewise linear approximation that greatly improves the geometrical faithfulness of the method. A comparison of various methods for tracking interfaces is given in [29].

Recently, in order to understand the gas-liquid interaction through a turbulent free-surface in a high wind velocity range, Kunugi [30] has developed a precise free-surface tracking algorithm, that is, Multi-interfaces Advection and Reconstruction Solver (MARS), and performed an accurate three-dimensional DNS of a turbulent field including both of the gas- and liquid-flows. In case of large amplitude deformation of a free-surface under a strong shear stress, they also showed that the velocity fluctuation normal to the free-surface is larger than that in the spanwise derection in the free-surface region [31, 32]. Their results suggest that the vertical velocity component produced by the wavy or turbulent fluctuations of the free surface contributes to enhance the momentum, heat and passive scalar transport across the interface.

Yabe and Xiao [33, 34] developed an interface tracking technique that is numerically efficient, geometrically faithful, and diffusionless. It is a combined method of the cubic-interpolated pseudo-particle (CIP) advection solver and a tangent function transformation. The CIP-combined, unified procedure (C-CUP) [35] based on the CIP scheme is applied to the two-phase flow problem, where the compressible and incompressible fluids can be treated simultaneously, in the same code. Even in cases that an interface is largely deformed by a strong wind shear, the C-CUP method can resolve the complicated interfaces on the Cartesian coordinates. One of the advantages in the C-CUP method is that a multi-phase flow with the phase-change can be accurately simulated by calculating the local sound speed at each numerical cell. Since it is not necessary to reconstruct the numerical grid in the C-CUP method, the numerical cost and errors can also be reduced in comparison to MARS. Using the C-CUP method, Mutsuda et al. [36, 37] succeeded in performing a DNS of wave-breaking and entrained air bubble in a gas-liquid turbulent layer. However, there has been no quantitative evaluation of the friction stress by means of the two-phase flow simulation.

1.4 Objectives in This Study

By use of the DNS of the two-phase flow involving a gas-liquid interface, behaviors of a

gas-liquid interface can be investigated more in detail than the conventional empirical model. It is important to understand the interactions of the free-surface and the wind in order to clarify the exchange processes of the physical quantities between the wind-wave and the turbulent liquid flow. Toba [19] has found the 3/2-law of the wind-waves from the similarity of energy spectra, which are obtained by wind-tank experiments and the field observations. Before applying the numerical model of a two-phase flow to Atmosphere and Ocean system, it is necessary to quantitatively evaluate accuracy of the friction stress on the free-surface given by the simulation in comparison to the tank experiments and the field observations.

The objective of this study is to show the validity of the numerical method based on the C-CUP scheme, by quantitatively comparing the simulation results with experimental data, towards construction of a reliable method for evaluating the friction stress between Atmosphere and Ocean. In this study, it is aimed not only to clarify the fundamental physical processes, but also to derive meaningful information for studying the large scale interactions between Atmosphere and Ocean. The reasons for adopting the C-CUP method are summarized as follows. First, applicability of the C-CUP method to the compressible fluid has an advantage in simulation of severe phenomena such as a typhoon. Second, the C-CUP method can keep thickness of a transition region near the sea-surface compact, which is important in long-term integration. Moreover, it is a more direct way to solve the same equations for both Atmosphere and Ocean, as is done in the C-CUP method, than treating them separately through boundary conditions on the sea-surface.

In this study, the numerical domain is selected similar to tank-experiments, where the depth is almost consistent with that of the tank-experiments [7, 8], so as to directly compare the simulation results with the experiments. Results of the two-phase flow simulations are analyzed in focus on the turbulent statistics. A transfer mechanism of the turbulent energy from the gas to the liquid is discussed by noting the Reynolds stress which is produced over the fluctuating free-surface. The friction velocity obtained by the simulation shows a quantitative agreement with experimental data.

This paper is organized as follows. In section 2, a review of the CIP method and the numerical techniques used in the two-phase flow simulation are described. In section 3, the C-CUP method used in the two-phase flow simulation is explained, and their numerical procedure and the results of several numerical test problems are presented. In section 4, the simulation results for open-channel turbulence are discussed. Finally, in section 5, the simulation results for the two-phase flow are discussed, and quantitative evaluation of the friction stress is compared with the experiments in order to show the validity of the numerical method used in this study.

2 A Brief Review of CIP Methods

2.1 CIP Algorithms for Advection Equation

2.1.1 Basic Algorithm

A review of the CIP method [35] in one dimensional case is shown bellow. This method is a numerical solver for a convection equation:

$$\frac{\partial f}{\partial t}+u\frac{\partial f}{\partial x}=0 \tag{2.1}$$

where f is a dependent variable and u is a convection velocity. The solution of Eq. (2.1) gives a simple transitional motion of wave with the velocity u. If we differentiate Eq. (2.1) with the spatial variable x, we obtain

$$\frac{\partial f'}{\partial t}+u\frac{\partial f'}{\partial x}=-\frac{\partial u}{\partial x}f' \tag{2.2}$$

where $f'=\partial f/\partial x$. In the simplest case where the velocity u is constant, Eq. (2.2) has the same form as Eq. (2.1) and represents the propagation of f' with the velocity u. By these equations, we can trace time evolutions of f and f'. If f' propagates with f, the profile after one time-step is limited to a specific one. It is imagined that, by this limitation, the solution becomes much closer to the initial profile.

If two values of f and f' are given at two grid points, the profile between these points can be described by a cubic polynomial

$$F_i(x)=a_iX^3+b_iX^2+f_i'X+f_i \tag{2.3}$$

where $X=x-x_i$. If the values of f and f' at all grid points are known, we have two parameters a_i, b_i to be determined. These parameters are determined by the condition that f and f' at point x_{i+1} given by Eq. (2.3), are equal to f_{i+1}, f_{i+1}', respectively. Then, one finds

$$a_i=\frac{f_i'+f_{iup}'}{D^2}+\frac{2(f_i-f_{iup})}{D^3} \tag{2.4}$$

$$b_i=-\frac{2f_i'+f_{iup}'}{D}+\frac{3(f_{iup}'-f_i')}{D^2} \tag{2.5}$$

where $D=-\Delta x\cdot\mathrm{sgn}(u_i)$ and $iup=i-\mathrm{sgn}(u_i)$. Also, $\mathrm{sgn}(u_i)$ means sign of u_i, such that $\mathrm{sgn}(u_i)=1$ for $u_i>0$ and $\mathrm{sgn}(u_i)=-1$ for $u_i<0$. At an intermediate time-step denoted by *, the value f* and the spatial derivative f'* are given by

$$f_i^*=F_i(x_i-u_i\Delta t)=a_i\xi^3+b_i\xi^2+f_i'\xi+f_i \tag{2.6}$$

$$f_i'^{*} = \frac{dF_i(x_i - u_i \Delta t)}{dx} = 3a_i\xi^2 + 2b_i\xi + f_i' \tag{2.7}$$

where $\xi = -u_i \Delta t$. The key of the CIP method is in the way of determining the time evolution of the spatial derivative f' by use of Eq. (2.2). Therefore, the profile even in a grid cell is defined within the accuracy of the interpolation method in Eq. (2.3).

In Fig. 2.1, three numerical schemes are compared for a typical problem of square and triangle wave propagation with CFL=0.5, where the profiles after 2000 steps are plotted. In the first-order upwind scheme shown in Fig. 2.1 (a), the initial sharp profile is smoothed out due to the numerical diffusion. In the Lax-Wendroff scheme shown in Fig. 2.1 (b), overshooting and a phase error are significantly observed. In the CIP scheme shown in Fig. 2.1 (c), the sharpness of the initial profile is successfully preserved but with small overshooting on the shoulders of the square wave. The small-scale errors, however, do not grow substantially in time.

The CIP method can be extended into two- and three-dimensions in a straightforward way. The governing equations for spatial derivatives f' in multidimensions are derived by differentiating the advection equation with respect to the spatial coordinates. By use of a special treatment of the first derivatives of the interpolation function, the CIP method can be constructed in a compact form where only one mesh cell is employed for the interpolation while keeping the resolution in a subcell-scale.

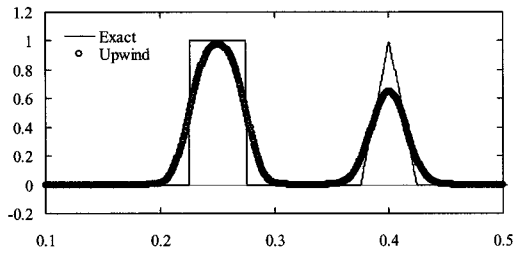

(a) First-order upwind scheme

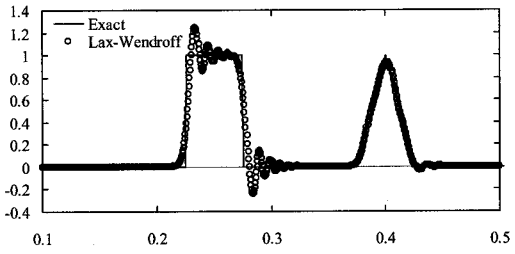

(b) Lax-Wendroff scheme

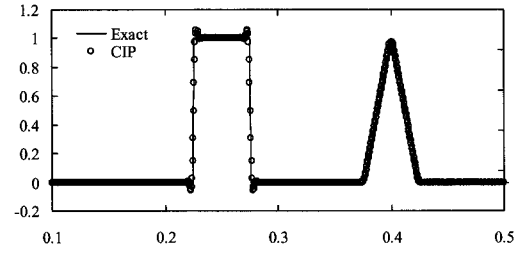

(c) CIP scheme

Figure 2.1: Profiles after 2000 steps for the propagation of square and triangle waves.

2.1.2 Rational CIP Method

A numerical scheme free from the artificial diffusion and oscillation is preferable in simulations of the advection equation. In modern Eulerian schemes with high resolution, in order to eliminate spurious oscillations, numerical viscosity is usually introduced. The artificial manipulation degrades the accuracy of the scheme when discontinuities exist. Preserving the shape of the advected field is aimed in the semi-Lagrangian schmes, since a scheme with a higher-orders interpolator than the second one often suffer from spurious numerical oscillations near at steep gradients or discontinuities.

In the original CIP method with the cubic polynomial interpolant [35], numerical oscillations are generated near the area where the dependent variable has a degree of smoothness less than unity. A shape-preserving scheme implemented with a CIP-type method was developed by means of a rational interpolation function. It is called the RCIP (rational-cubic interpolation propagation) scheme [38, 39], and shows good properties in keeping the topological nature of data, namely, in preserving convexity or concavity.

Since the original CIP method causes the numerical oscillations near the discontinuities, its application to the two-phase flow simulation may lead to negative values of the density and/or pressure near at the gas-liquid interface. Then, the numerical instability may occur. Therefore, the rational CIP method is used for the advection equations in the present two-phase flow simulations.

The one dimensional RCIP scheme is based on the rational function [38, 39], which interpolates the profile such as

$$R_i^{1D}(x) = \left(\sum_{0 \le p \le 1} \alpha_p \beta_p X^p \right)^{-1} \sum_{0 \le lx \le 3} C_{lx} X^{lx} , \tag{2.8}$$

where $X = x - x_i$ and

$$C_0 = f_i$$

$$C_1 = g_i + f_i \alpha_1 \beta_1$$

$$C_2 = S_i \alpha_1 \beta_1 + (S_i - d_i)\Delta_i^{-1} - C_3 \Delta_i$$

$$C_3 = [g_i - S_i + (g_{iup} - S_i)(1 + \alpha_1 \beta_1 \Delta_i)]\Delta_i^{-2}$$

$$\alpha_0 = 1.0$$

$$\beta_0 = 1.0$$

$$\beta_1 = [\,|(S_i - g_i)/(g_{iup} - S_i) - 1\,|]\Delta_i^{-1} .$$

A control parameter $\alpha_1 \in [0,1]$ is also introduced in Eq. (2.8). The other notations are defined as

$$\Delta_i = x_{iup} - x_i$$

$$S_i = (f_{iup} - f_i)\Delta_i^{-1}$$

$$g_i = (df/dx)_i$$

In deriving the above coefficients, we first determined β_1 by setting $C_3 = 0$, which means a second-order polynomial is used in the numerator of Eq. (2.8). Thus, β_1 should strongly works at the discontinuity where effective accuracy of the scheme becomes a lower order. Four constraints for f and g at neighboring points are sufficient to determine these coefficients. After obtaining β_1, we use it as a fixed value so as to find C_3, and uniquely determine the cubic polynomial for the four constraints on f and g.

Then a solution to the advection equation can be written as

$$f_i^{n+1} = R_i^{1D}(x_i - u\Delta t) = \frac{C_0 + C_1\xi + C_2\xi^2 + C_3\xi^3}{1 + \alpha_1\beta_1\xi}, \tag{2.9}$$

and the first-order derivative of the dependent variable is calculated by

$$g_i^{n+1} = \partial_x f_i^{n+1} = \partial_x R_i^{1D}(x_i - u\Delta t) = (C_1 + 2C_2\xi + 3C_3\xi^2)(1+\alpha_1\beta_1\xi)^{-1}$$

$$-\alpha_1\beta_1(C_0 + C_1\xi + C_2\xi^2 + C_3\xi^3)(1+\alpha_1\beta_1\xi)^{-2} - \left(\frac{\partial u}{\partial x}\frac{\partial f}{\partial x}\right)_i^n, \tag{2.10}$$

where $\xi = -u\Delta t$. All the coefficients in the above expressions are computed from the quantities of f and g at the time-step n. It is interesting to see that the second term on the right-hand side of Eq. (2.10) is proportional to $-\alpha_1\beta_1$ and hence plays a role in reducing the contribution of the third order polynomial term, $\alpha_1\beta_1 C_3\xi^3$, to g at the discontinuity.

The interpolation function (2.8) works like a third-order accurate scheme where the profile is smooth or α_1 is zero, while it behaves as a real rational function that suppresses oscillations in the neighborhood of discontinuities. The parameter $\alpha_1 \in [0,1]$ provides ones flexibility for changing a blending of the rational function and the cubic polynomials for interpolation. When the control parameter α_1 is set to be zero, the RCIP algorithm given in Eqs. (2.9) and (2.10) are identical to the original CIP method. For $\alpha_1 = 1$, convex-concave and monotone of f are preserved as proved in [38], if the given function f is nonconcave or nonconvex,.

Numerical experiments, shown in Fig. 2.2 demonstrate that the scheme of Eqs. (2.9) and (2.10) is capable of suppressing the spurious oscillation near discontinuities. Obviously, in the scheme with $\alpha_1 = 1$ as shown in Fig. 2.2 (b), no oscillation is observed, although the original CIP method with α_1=0 as shown in Fig. 2.2 (a) produces small overshooting on the shoulders of the square wave.

Two- and three-dimensional schemes can also be constructed by use of the following interpolation functions [39].

$$R_i^{2D}(x,y)=\left(\sum_{0\le p+q\le 1}\alpha_{p,q}\beta_{p,q}X^pY^q\right)^{-1}\sum_{0\le {}^lx+{}^ly\le 3}C_{{}^lx,{}^ly}X^{{}^lx}Y^{{}^ly}, \tag{2.12}$$

and

$$R_i^{3D}(x,y,z)=\left(\sum_{0\le p+q+r\le 1}\alpha_{p,q,r}\beta_{p,q,r}X^pY^qZ^r\right)^{-1}\sum_{0\le {}^lx+{}^ly+{}^lz\le 3}C_{{}^lx,{}^ly,{}^lz}X^{{}^lx}Y^{{}^ly}Z^{{}^lz}, \tag{2.13}$$

In order to reduce the oscillations near the discontinuities, i.e. the gas-liquid interface, and to avoid the negative values of the density and/or pressure, the control parameter α_1 is set to unity in the present study.

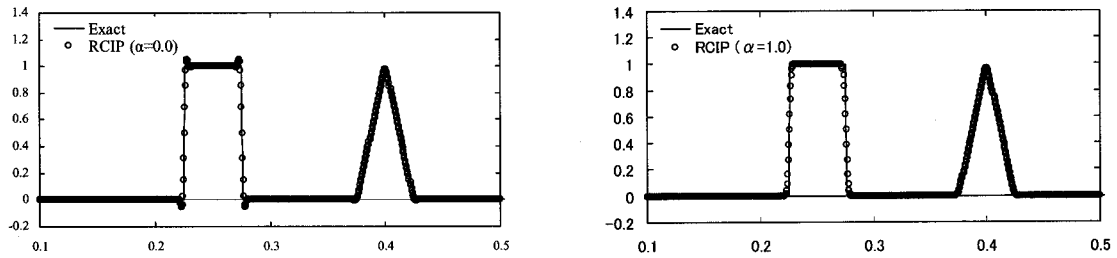

(a) Original CIP method ($\alpha_1=0$) (b) RCIP scheme ($\alpha_1=1$)

Figure 2.2: Profiles after 2000 steps for the propagation of square and triangle waves.

2.1.3 Tangent Transformed CIP Method

As shown in the previous section, the rational CIP method can reproduce the solutions with no numerical oscillation near the discontinuities, by introducing weak numerical diffusion. In the two-phase flow simulation, it is important to keep the thickness of a transition region near the gas-liquid interface compact, in order to simulate the transfer process through the interface accurately. Thus, it is necessary to reduce the numerical diffusion and to keep the compactness of the interface region. Therefore, in this study, the tangent transformed CIP method proposed by Yabe and Xiao [33] is used in the advection equation for the density function that defines the transition region.

The tangent transformed CIP method [40] is explained bellow. Consider K kinds of impermeable materials occupying closed areas $\{\Omega_k(t),\ k=1,2,...,K\}$ in a computational domain $D\in\mathbf{R}^3(x,y,z)$. We identify them with density functions $\{\phi_k(x,y,z,t),\ k=1,2,...,K\}$ according to the following definition,

$$\phi_k(x,y,z,t)=1,\ (x,y,z)\in\Omega_k(t),$$
$$=0,\ otherwise. \tag{2.14}$$

Suppose these materials move with the local velocity $\mathbf{u}$; then the density function evolve according

to the advection equation

$$\frac{\partial \phi_k}{\partial t} + \mathbf{u} \cdot \nabla \phi_k = 0, \; k = 1,2,...,K . \tag{2.15}$$

In this method, instead of the original variable ϕ_k, its transformation, $F(\phi_k)$, is calculated by the CIP method. When $F(\phi_k)$ is a function of ϕ_k only, the new function $F(\phi_k)$ is also governed by the same equation as (2.15). Hence, we have

$$\frac{\partial F(\phi_k)}{\partial t} + \mathbf{u} \cdot \nabla F(\phi_k) = 0, \tag{2.16}$$

which means that the algorithms proposed for ϕ_k can be used for $F(\phi_k)$. Considerable simplicity of this kind of technique is attractive in practical implementation. A transformation by a tangent function is considered to be useful.

$$F(\phi_k) = \tan[(1-\varepsilon)\pi(\phi_k - 1/2)], \tag{2.17}$$

$$\phi_k = \tan^{-1} F(\phi_k)/[(1-\varepsilon)\pi] + 1/2, \tag{2.18}$$

where ε is a small positive constant. Introduction of the small parameter ε enables us to avoid the divergence of $F(\phi_k)$ [$F(\phi_k) = -\infty$ for $\phi_k = 0$ and $F(\phi_k) = \infty$ for $\phi_k = 1$ if $\varepsilon = 0$] and control steepness of the transition layer.

Even if ϕ_k rapidly changes from 0 to 1 at the interface, $F(\phi_k)$ shows a regular behavior. Because the value of $F(\phi_k)$ evaluated near at $\phi_k = 0$ and 1 smoothly varies, the tangent function transformation can locally improve the spatial resolution near the steep gradients. Thus, the sharp discontinuity can be easily described on numerical grids. This kind of transformation is effective only for the case where the value of ϕ_k is limited to a finite range throughout the calculation, such as the density function defined above. This method does not involve any interface construction procedure, and hence, is economical in computational costs. One of the interesting applications of the tangent transformation method is the shock-wave interaction with a liquid drop, where a deformable shape of the drop has been successfully captured [33]. It is also advantageous that the extension of the above scheme to multi-dimensions is straightforward.

Fig. 2.3 shows simulation results of two-dimensional rotation of a solid body. The computational conditions are the same as those used by Zalesak [41]. Inside a 100×100 grid system, a sphere with radius of 15 grids and a slit of 5 grids is located at (x, y) = (0,75). This shape rotates around the center at (50, 50) in 628 time steps for one rotation. It can be seen that the shape is almost preserved by the tangent transformed CIP method, while the result from the original CIP scheme shows numerical diffusion. It should be emphasized the successful result in Fig. 2.3(c) is obtained without introduction of any flux-limiting procedure which is often used in most of modern schemes.

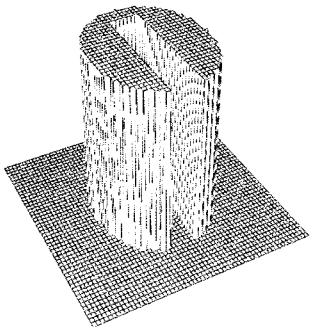

(a) Initial profile

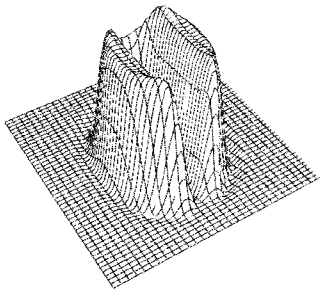

(b) CIP scheme

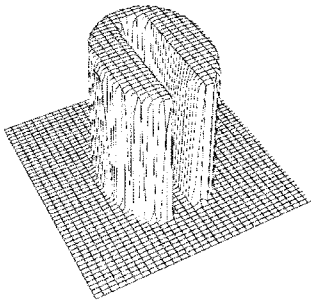

(c) Tangent transformed CIP method

Figure 2.3: Perspective plots of a solid body in a two dimensional plane after one rotation with 628 steps.

2.2 Treatment of Other Terms

2.2.1 Pressure-Based Algorithm

In the CIP method, formulations commonly used both for the incompressible and compressible fluids have been obtained. In the compressible case, the density ρ is solved by the mass conservation equation. Then, the temperature T is obtained by the energy equation. After that, from the equation of state (EOS), the pressure $p = p(\rho, T)$ is calculated. When the density is low, the pressure is proportional to ρT, $p \propto \rho T$, like the ideal gas with a dependence of p on ρ. The solid or liquid pressure, however, steeply rise as the density increases. This means that extremely high pressure is needed to compress a solid or a liquid even slightly. In other words, the sound speed in a solid as well as a liquid, $C_s = (\partial p / \partial \rho)^{1/2}$ is quite large. Therefore, even if the density calculation has only a small amount of error, say 10%, it may cause a large pressure pulse of 3-4 orders of magnitude. In such a situation, the incompressible approximation is normally adopted, where the pressure equation ensuring $\nabla \cdot \mathbf{u} = 0$ is derived from the equation of motion and the mass conservation. This type of method is called a pressure-based scheme; MAC [42], SMAC [43],

SIMPLE [44], and SIMPLER [45] are typical examples.

In order to resolve the above problem in the compressible fluid, it is necessary to modify the EOS. If the pressure is solved first to estimate the density in terms of $\rho(p,T)$ by using the EOS, the problem at liquid density would be avoided. In addition, since the EOS in the low density gas depends linearly on other quantities, this reverse procedure causes no problem even in that case. For realization of this reverse procedure, it should be determined how the pressure reacts to changes in density and temperature. The first unified-procedure to incorporate the compressible fluid with incompressible one has been considered by Harlow and Amsden, that is the ICE (implicit continuous Eulerian) method [46] which has also been improved in the PISO (pressure implicit with splitting of operators) scheme [47]. In both cases, conservative forms are used as a starting point. The main difference between ICE and PISO is in treatment of the convection term.

On the other hand, in the C-CUP method [35], Euler equations are employed with splitting of the advection term from the others associated with sound waves. This scheme also simplifies the pressure equation and greatly improves applicability to the multiphase flow. Zienkiewicz [48] proposed a similar procedure but applied it to the finite-element method. However, with their scheme, it is not easy to remove the difficulty stemming from a large density ratio near at boundary between a liquid and a gas, as discussed below.

In both the ICE and the PISO, conservation equations of mass and momentum are used in a finite-difference form,

$$\frac{\rho^{n+1}-\rho^{n}}{\Delta t}=-\frac{\partial(\rho u)'}{\partial x} \tag{2.19}$$

$$\frac{(\rho u)'-(\rho u)^{n}}{\Delta t}=-\frac{\partial p^{n+1}}{\partial x}+H(u) \tag{2.20}$$

$$H(u)\equiv-\frac{\partial(\rho u^{2})}{\partial x}. \tag{2.21}$$

Substituting Eq. (2.20) into Eq. (2.19), one finds

$$\frac{\partial^{2} p^{n+1}}{\partial x^{2}}=\frac{\rho^{n+1}-\rho^{n}}{\Delta t^{2}}+\frac{1}{\Delta t}\left(\frac{\partial(\rho u)}{\partial x}\right)^{n}+\frac{\partial H(u)}{\partial x}. \tag{2.22}$$

Next, if it is assumed that the density changes in proportion to the pressure change,

$$\Delta p=\left(\frac{\partial p}{\partial \rho}\right)_{T}\Delta\rho=C_{s}{}^{2}\Delta\rho \tag{2.23}$$

the density variation on the right-hand side of Eq. (2.22) can be replaced by that of the pressure,

$$\frac{\partial^{2} p^{n+1}}{\partial x^{2}}=\frac{p^{n+1}-p^{n}}{C_{s}{}^{2}\Delta t^{2}}+\frac{1}{\Delta t}\left(\frac{\partial(\rho u)}{\partial x}\right)^{n}+\frac{\partial H(u)}{\partial x} \tag{2.24}$$

In the ICE method, the term with $H(u)$ is estimated at the nth time-step. In the PISO scheme, it is predicted by an equation of motion

$$\frac{\rho^n u^P - (\rho u)^n}{\Delta t} = -\frac{\partial p^n}{\partial x} + H(u^P). \tag{2.25}$$

Thus, one finds

$$\frac{\partial^2 (p^{n+1} - p^n)}{\partial x^2} = \frac{p^{n+1} - p^n}{C_s{}^2 \Delta t^2} + \frac{1}{\Delta t}\left(\frac{\partial(\rho^n u^P)}{\partial x}\right)^n. \tag{2.26}$$

The original PISO is more complicated than that given above, because the predictor-corrector algorithm is incorporated with diagonalization of the $H(u)$ term for finding u^P from Eq. (2.25).

2.2.2 C-CUP Method

Yabe and Wang [35] adopted the Euler form instead of the conservative representation for the pressure equation. Furthermore, the advection terms are separated from the others, since the advection term can be processed free from the CFL condition in the semi-Lagrangian type procedure including the CIP scheme. Fortunately, the splitting method has a benefit to solving the multiphase flow equations, as shown below.

The C-CUP method, which was originally proposed for the EOS in the form of Eq. (2.23), is extended to a more general type of EOS [49]. For small variations of density and temperature, the pressure change will be linearly proportional to them, such that

$$\Delta p = (\partial p / \partial \rho)_T \Delta \rho + (\partial p / \partial T)_\rho \Delta T, \tag{2.27}$$

where Δp means the pressure change, $p^{n+1} - p^*$, during one time-step. Asterisk * denotes the value obtained after separately solving the advection. The same procedure is also applied to ρ and T. From this relation, once $\Delta\rho$ and ΔT are predicted, Δp is given by Eq. (2.27) with $\partial p / \partial \rho$ and $\partial p / \partial T$ determined by the EOS.

In the followings, we concentrate on treatment of the non-advection terms related to sound waves. They are the primary cause of the difficulty in solving the liquid motion while retaining the compressibility. Suppose, $\Delta\rho$ and ΔT are simply given by

$$\Delta\rho = -\rho^* \nabla \cdot \mathbf{u}^{n+1} \Delta t \quad \text{and} \quad \rho^* C_v \Delta T = -P_{TH} \nabla \cdot \mathbf{u}^{n+1} \Delta t, \tag{2.28}$$

where C_v is the specific heat at a constant volume, and $\mathbf{u}^{n+1}$ is defined by the equation of motion,

$$\Delta \mathbf{u} = -\frac{\nabla p^{n+1}}{\rho^*} \Delta t, \tag{2.29}$$

with $\Delta \mathbf{u} = \mathbf{u}^{n+1} - \mathbf{u}^*$. Equations (2.27)-(2.29) with $C_s{}^2 = (\partial p / \partial \rho)_T$ and $P_{TH} = T(\partial p / \partial T)_\rho$ lead to an equation for the pressure at the (n+1)th time-step [35, 49],

$$\nabla\left(\frac{\nabla p^{n+1}}{\rho^*}\right)=\frac{p^{n+1}-p^*}{\Delta t^2\left(\rho^* C_s^{\,2}+\dfrac{P_{TH}^{\,2}}{\rho^* C_v T}\right)}+\frac{\nabla\cdot\mathbf{u}^*}{\Delta t}. \tag{2.30}$$

Then substituting p^{n+1} into Eq. (2.29), the velocity $\mathbf{u}^{n+1}$ can be obtained. Then, the density ρ^{n+1} is calculated from Eq. (2.28). Equation (2.30) has many important features. This equation is based on the fact that the normal component of the acceleration $n\cdot(\nabla p/\rho)$ is continuous at sharp discontinuities, while the density changes by several orders of magnitude at the boundary between a liquid and a gas. In this case, since the denominator of $\nabla p/\rho$ changes by several orders, the pressure gradient must be calculated with high accuracy so as to ensure the continuous change of the acceleration. Although Eq. (2.24) and (2.26) seem to be similar to Eq. (2.30), the continuity of $\nabla p/\rho$ is not guaranteed in the ICE and the PISO. In contrast, Eq. (2.30) works robustly even with a density ratio larger than 1000, and enables ones to treat the compressible and incompressible fluids simultaneously. Computationally, the solution of Eq. (2.30) provides a pressure distribution that can be used to project the velocity field on a variable density flow; i.e., the resulting pressure field is weighted by the inverse density. Other projection methods with variable density for the incompressible fluid can be found in Refs. [27] and [50].

3 C-CUP Method Used in Free-Surface Flow Simulations

3.1 Governing Equations and Their Numerical Modeling

The governing equations for the present numerical simulations for free-surface flows are given by the compressible Navier-Stokes equation, the continuity equation, the pressure equation and the advection equation of the density function, that is,

$$\rho\left(\frac{\partial u_i}{\partial t}+u_j\frac{\partial u_i}{\partial x_j}\right)=-\frac{\partial P}{\partial x_i}+\mu\frac{\partial^2 u_i}{\partial x_j\partial x_j}+\frac{1}{3}\mu\frac{\partial}{\partial x_i}\frac{\partial u_j}{\partial x_j}+g_{i2}+F_i, \tag{3.1}$$

$$\frac{\partial\rho}{\partial t}+\frac{\partial(\rho u_i)}{\partial x_i}=0, \tag{3.2}$$

$$\frac{\partial P}{\partial t}+u_i\frac{\partial P}{\partial x_i}+\rho C_s{}^2\frac{\partial u_i}{\partial x_i}=0, \tag{3.3}$$

$$\frac{\partial\phi}{\partial t}+u_i\frac{\partial\phi}{\partial x_i}=0. \tag{3.4}$$

Here, repetition of the same subscript means the summation convention, and g, μ, C_s, ϕ and F_i denote the gravitational constant, the viscosity coefficient, the local sound speed, the density function and the surface tension, respectively. The continuum surface force (CSF) model, which is often used in two-phase flow simulations, proposed by Brackbill et al. [51] is applied to the surface tension. This model for the surface tension transforms a pressure difference acting to the interface into a body force. In the above set of equations, the advection equation of the density function is employed while the continuum equation of the density function was used by Mutsuda [36]. All variables are normalized by the depth δ and the friction velocity at the wall. As listed in Table 3.1, all parameters are consistent with those of real air and water, and the pressure is set to be the sea-level one. The procedure of the C-CUP method is summarized as follows; the advection terms in Eqs. (3.1)-(3.4) are integrated in time by CIP method, and then, other terms are calculated after solving the Poisson equation for the pressure, as explained in Chapter 2.

In a transition region near the free-surface, the local sound speed is modeled by a linear weighting the function $C_s=C_{s,Liq}\phi+C_{s,Gas}(1-\phi)$. Here we define $\phi=1$ for liquid-phase, $\phi=0$ for gas-phase and $0<\phi<1$ for the gas-liquid interface region. The viscous coefficient is modeled by an inversely proportional relation $1/\mu=1/\mu_{Liq}\phi+1/\mu_{Gas}(1-\phi)$ which shows a better property than the linear relation and agrees with experimental data for two-phase mixing fluids by McAdams et al. [52] as shown in Fig. 3.1. By use of the numerical model given above, it is possible to simulate the two-phase flows of the gas and the liquid without any complicated boundary conditions at the interface.

Table 3.1: Numerical parameters.

Gravitational constant	9.80665 [m/s^2]
Reference pressure	1000 [hPa]
Gas density	1.2 [kg/m^3]
Liquid density	1000 [kg/m^3]
Gas viscous coefficient	1.8×10^{-5} [Pa·s]
Liquid viscous coefficient	1.0×10^{-3} [Pa·s]
Surface tension coefficient	7.2×10^{-2} [Pa/m]

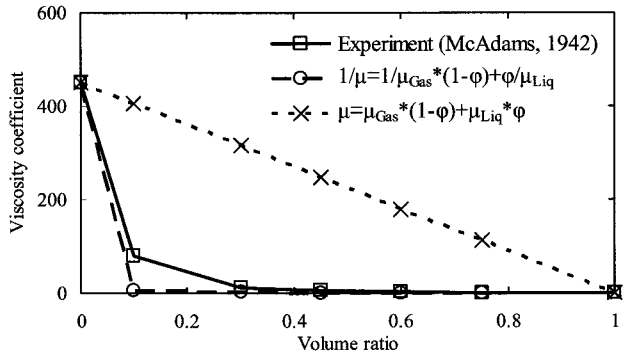

Figure 3.1: Viscosity coefficient modeled by various ways.

3.2 Numerical Model of Surface Tension

The CSF model [51] is widely used in CFD (computational fluid dynamics), where the surface tension is represented in a form of a volume force. The model surface force is proportional to the product of the interface gradient and the surface curvature.

First, consider an effect of the surface tension on a fluid interface. The boundary condition with the surface stress at an interface between two fluids (labeled 1 and 2) is [53]

$$(p_1 - p_2 + \sigma\kappa)\hat{n}_i = (\tau_{1,ik} - \tau_{2,ik})\hat{n}_k + \frac{\partial\sigma}{\partial x_i}, \tag{3.5}$$

where σ is the fluid surface tension coefficient in units of force per unit length, p_α is the pressure in fluid α for α=1 or 2. The viscous stress tensor and the outward unit normal to the fluid 2 at the interface are denoted by $\tau_{\alpha,ik}$ and $\hat{n}_i$, respectively. The local surface curvature, κ, which is represented as

$$\kappa = \frac{1}{R_1} + \frac{1}{R_2}. \tag{3.6}$$

where R_1 (R_2) is the radius of curvature of the fluid 1 (2).

Brackbill et al. [51] proposed an accurate model of the normal boundary condition at interfaces between inviscid incompressible fluids ($\mu = 0$), where the surface tension coefficient σ is constant. This condition reduces to Laplace's formula [53] for the surface pressure p_s which is given by a jump of the fluid pressure across an interface with a surface tension,

$$p_s \equiv p_2 - p_1 = \sigma\kappa . \tag{3.7}$$

The surface pressure is, thus, proportional to the curvature κ of the interface. The higher pressure is in the fluid medium on the concave side of the interface, since the surface tension results in a net normal force directed toward the center of curvature of the interface. Normal component of the surface force per unit interfacial area A at a point $\mathbf{x}_s$ can then be written as

$$F_{sa}^{(n)}(\mathbf{x}_S) = \sigma\kappa(\mathbf{x}_S)\hat{n}(\mathbf{x}_S) \tag{3.8}$$

where the curvature $\kappa(\mathbf{x}_S)$ is taken positive, if the center of curvature is in fluid 2, and if the unit normal is assumed to point into fluid 2.

Now, let us consider two fluids (fluid 1 and 2), separated by an interface at time t. The two fluids are distinguished by the color function or the density function $\phi(\mathbf{x})$. Thickness of the transition region is of the order of the grid spacing h. Except in the transition region, $\phi(\mathbf{x})$ has the values of ϕ_1 (ϕ_2) in fluids 1 (2). The interface between the fluids is given by the surface $\phi(\mathbf{x}_S) = (1/2)(\phi_1 + \phi_2) \equiv <\phi>$. Contours of constant values of the color function are shown in Fig. 3.2, where a smooth variation of $\phi(\mathbf{x})$ given by interpolation is illustrated. The interface represented by the transition region is not aligned with the grid. In the transition region, there are nested contours of $\phi(\mathbf{x})$, where $\phi_1 \le \phi \le \phi_2$.

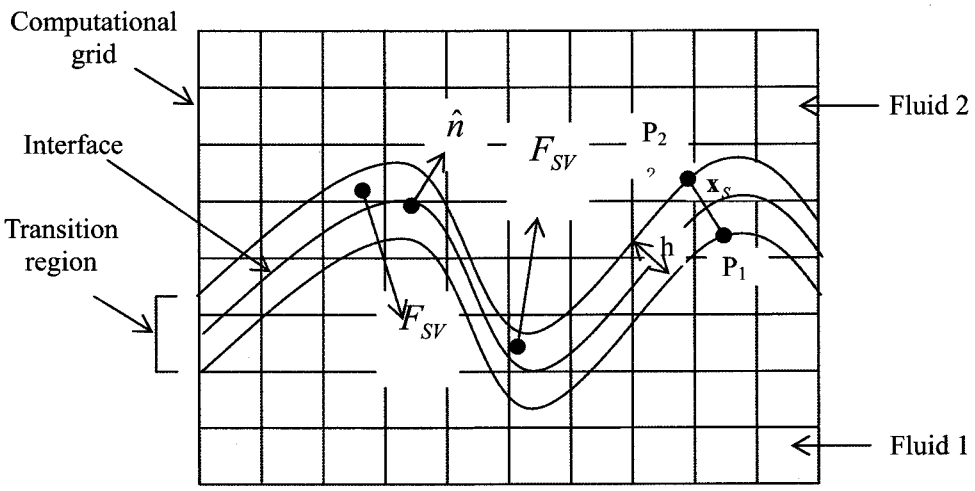

Figure 3.2: Illustration of the contours of constant color function and the interface force modeled by CSF model.

In the color function model given above, the interface where the kind of fluids changes from 1 to 2 is represented by a continuous transition. It is no longer appropriate to apply the pressure jump induced by the surface tension at an interface. The surface tension should, rather, act on every fluid element in the transition region. Consider a volume force $F_{SV}(\mathbf{x})$ that gives the correct surface tension force per unit interfacial area $F_{Sa}(\mathbf{x}_s)$ as $h \to 0$,

$$\lim_{h\to 0} \int_{\Delta V} F_{SV}(\mathbf{x}) d^3x = \int_{\Delta A} F_{Sa}(\mathbf{x}_s) dA, \tag{3.9}$$

where the area integral is taken over the portion ΔA of the interface locating in the small volume ΔV. The volume element ΔV is defined so that its edges are normal to the interface, and that its thickness h is much smaller than the radius of curvature of the interface A. Then, the Lagrangian fluid momentum equation for an inviscid fluid with the surface tension is approximated by

$$\rho \frac{d\mathbf{u}}{dt} = -\nabla p - F_{SV}, \tag{3.10}$$

where ρ, $\mathbf{u}$, and p are the density, the velocity, and the pressure, respectively.

The integral of the normal component of $\nabla\phi(\mathbf{x})$ across the interface is given by

$$\lim_{h\to 0} \int \hat{n}(\mathbf{x}_S) \nabla\phi(\mathbf{x}) dx = [\phi]. \tag{3.11}$$

where $[\phi] = \phi_2 - \phi_1$. In the gas-liquid flow condition, we choose $\phi_2 = 1$ for the liquid and $\phi_1 = 0$ for the gas. Thus, in the limit of $h \to 0$, $\nabla\phi(\mathbf{x})$ can be written as

$$\lim_{h\to 0} \nabla\phi(\mathbf{x}) = \hat{n}(\mathbf{x}) \cdot [\phi] \delta[\hat{n}(\mathbf{x}_S) \cdot (\mathbf{x} - \mathbf{x}_S)]. \tag{3.12}$$

The delta function can be used to rewrite the surface integral of $F_{Sa}(\mathbf{x}_s)$ defined in Eq. (3.9), to a volume integral form for $h = 0$:

$$\int_A F_{Sa}(\mathbf{x}_S) dA = \int_V F_{Sa}{}^{(n)}(\mathbf{x}) \delta[\hat{n}(\mathbf{x}_S) \cdot (\mathbf{x} - \mathbf{x}_S)] dx^3$$

$$= \int_V \sigma\kappa(\mathbf{x}) \hat{n}(\mathbf{x}) \delta[\hat{n}(\mathbf{x}_S) \cdot (\mathbf{x} - \mathbf{x}_S)] dx^3. \tag{3.13}$$

The delta function converts the integral of $F_{Sa}(\mathbf{x})$ over a volume V to surface integral of $F_{Sa}(\mathbf{x}_s)$ over A. Substituting Eq. (3.12) to Eq. (3.13), we find that

$$\int_A F_{Sa}(\mathbf{x}_S) dA = \lim_{h\to 0} \int \sigma\kappa(\mathbf{x}) \nabla\phi(\mathbf{x}) dx^3, \tag{3.14}$$

which provides us an approximation of the surface force $F_{Sa}(\mathbf{x}_s)$ for a finite thickness h of the transition region. By comparing Eq. (3.14) with Eq. (3.9), we obtain a useful expression of the volume force $F_{SV}(\mathbf{x})$ for finite h,

$$F_{SV}(\mathbf{x}) = \sigma\kappa(\mathbf{x}) \nabla\phi(\mathbf{x}). \tag{3.15}$$

Then, the fluid acceleration due to surface tension is modeled by a volume force which depends on

the gradient (not on the value) of the color function. Therefore, the momentum equation simply becomes,

$$\rho \frac{d\mathbf{u}}{dt} = -\nabla p - \sigma\kappa(\mathbf{x})\nabla\phi(\mathbf{x}). \tag{3.16}$$

The curvature κ of the interface A at $\mathbf{x}_s$ is calculated from

$$\kappa = -(\nabla \cdot \hat{n}), \tag{3.17}$$

where $\hat{n}$ is the unit normal to the surface. In the CSF model, the interface is replaced by nested surfaces of the continuous color function with normals given by its gradient,

$$\mathbf{n}(\mathbf{x}) = \nabla\phi(\mathbf{x}). \tag{3.18}$$

The unit normal is, thus,

$$\hat{n}(\mathbf{x}) = \frac{\nabla\phi(\mathbf{x})}{|\nabla\phi(\mathbf{x})|}. \tag{3.19}$$

It follows that the expression for $\kappa\nabla\phi$, which is needed to evaluate the surface volume force, is given by

$$\kappa\nabla\phi = -\mathbf{n}(\nabla \cdot \hat{n}), \tag{3.20}$$

where we have used Eq. (3.17) and Eq. (3.18). The surface volume force is also finite only in the transition region where $\nabla\phi$ has non-zero values.

Computing the curvature requires the gradient field of the color function ϕ. Using the CIP method in calculation of ϕ, one can simultaneously obtain the solutions to ϕ and its first-order derivatives. In evaluating the curvature κ, thus, the gradients of ϕ have been directly manipulated as dependent variables. The effects of the surface tension are consequently included in the computational model through a volume force term acting only in the transition region near the interface.

Eventually, if the unit normal $\hat{n}(\mathbf{x})$ and the curvature κ of the interface can be calculated, the volume force $F_{SV}(\mathbf{x})$ can be obtained. Consider how to calculate $\hat{n}(\mathbf{x})$ and κ using the color function ϕ in the two-dimensional case. One obtains face-centered components of the normal vector, by differentiating the color function ϕ in the neighboring cells,

$$n_{x,i+1/2,j} = \frac{\phi_{i+1,j} - \phi_{i,j}}{\Delta x}, \tag{3.21}$$

where $n_{x,i+1/2,j}$ means the x-component of $\hat{n}(\mathbf{x})$ at the right face $(i+1/2, j)$ of cell (i, j). Similarly,

$$n_{y,i,j+1/2} = \frac{\phi_{i,j+1} - \phi_{i,j}}{\Delta y}. \tag{3.22}$$

is the y-component at the top face $(i, j+1/2)$ of cell (i, j). Other components can be given by interpolation, such as

$$n_{x,i,j+1/2} = \frac{1}{4}\left(n_{x,i+1/2,j} + n_{x,i+1/2,j+1} + n_{x,i-1/2,j} + n_{x,i-1/2,j+1}\right), \tag{3.23}$$

for the x-component at the top face (i, j +1/2) of cell (i, j). Similarly, the y-component at faces of constant i must also be interpolated, such as

$$n_{y,i+1/2,j} = \frac{1}{4}\left(n_{y,i,j+1/2} + n_{y,i+1,j+1/2} + n_{y,i,j-1/2} + n_{y,i+1,j-1/2}\right), \tag{3.24}$$

for the y-component at the right face (i+1/2, j) of cell (i, j). The cell-centered normal vector, $\mathbf{n}_{i,j}$, is computed from the linear interpolation of the face-centered components in neighbors,

$$\mathbf{n}_{i,j} = \hat{x}\frac{1}{2}\left(n_{x,i+1/2,j} + n_{x,i-1/2,j}\right) + \hat{y}\frac{1}{2}\left(n_{y,i,j+1/2} + n_{y,i,j-1/2}\right), \tag{3.25}$$

Face-centered normal vector magnitudes are for example, given by,

$$\left|\mathbf{n}_{i+1/2,j}\right| = \left(n_{x,i+1/2,j}^2 + n_{y,i+1/2,j}^2\right)^{1/2} \tag{3.26}$$

for the right face (i+1/2, j) of cell (i, j), and

$$\left|\mathbf{n}_{i,j+1/2}\right| = \left(n_{x,i,j+1/2}^2 + n_{y,i,j+1/2}^2\right)^{1/2} \tag{3.27}$$

for the top face (i, j+1/2) of cell (i, j). A cell-centered curvature, $\kappa_{i,j} = -(\nabla\cdot\hat{\mathbf{n}})_{i,j}$, is calculated from the divergence of the face-centered unit normals,

$$(\nabla\cdot\hat{\mathbf{n}})_{i,j} = \frac{1}{\Delta x}\left(\frac{n_{x,i+1/2,j}}{\left|\mathbf{n}_{i+1/2,j}\right|} - \frac{n_{x,i-1/2,j}}{\left|\mathbf{n}_{i-1/2,j}\right|}\right) + \frac{1}{\Delta y}\left(\frac{n_{y,i,j+1/2}}{\left|\mathbf{n}_{i,j+1/2}\right|} - \frac{n_{y,i,j-1/2}}{\left|\mathbf{n}_{i,j-1/2}\right|}\right). \tag{3.28}$$

The above expression can be straightforwardly extended to the three-dimensional case.

3.3 Test Problems

3.3.1 Broken Dam Problem

In this subsection, we consider a benchmark test called the broken dam problem. In this example, a rectangular column of water in hydrostatic equilibrium is initially confined by two vertical walls in a two dimensional geometry. The collapse of a water column after removing one of the walls is calculated by our simulation code with the C-CUP method. Geometry of the initial water column is shown in Fig. 3.3. Laboratory experiments were carried out in the same geometry [54-56]. The height and the width of the water column are denoted by $2L$ and L, respectively. The water column is located on the left side of the simulation box with width of $4L$.

In the experiments by Koshizuka et al. [55] and Koshizuka et al. [56], the box is made of glass with the size of L=14.6cm. The initial water column is supported by a removable board, which is quickly slid up to start the collapse. Collapsing water impinges on the right vertical wall, which creates fragmentation and coalescence of the fluid.

The problem without the right vertical wall has been used for verification of the simulation

code for a free-surface flow. In this case, the shape of the free surface is assumed to be smooth so that grid methods can be applied. This is a good test problem because of its simple initial and boundary conditions. Free-surface motion both in the vertical and horizontal directions could be a useful check on capability of the present C-CUP method to treat a free surface flow.

In calculation of the collapse of a water column, the unit length L is set to 14.6cm as same as that of Koshizuka et al. [56]. Gravitational unit is 9.8m/s^2 and the pressure is set to be real Atmospheric pressure. The grid number is 80×60. The boundary conditions on the left, right, and bottom walls are free-slip. The surface tension is neglected.

In Fig. 3.4, distributions of the fluid resulted from the simulation are shown at 0.05s intervals from 0.0 to 0.25s. Motion of the leading edge, which is the front of the collapsing water running on the bottom wall, is shown in Fig. 3.5, where the calculated result is plotted by the solid line. The experimental data [54, 56] are presented as well. The calculated result agrees well with the experimental data, while the speed of the leading edge in the experiments is slightly slower than that of the simulation. The small difference is due to the friction between the fluid and the bottom wall. In the experiments by Koshizuka et al. [56], this friction effect is verified by a fact that the leading edge is rounded between the fluid and the bottom wall. Therefore, the result of the benchmark test suggests that the present C-CUP method can correctly represent free-surface motions in a two-phase flow system, such as a water flow in the air.

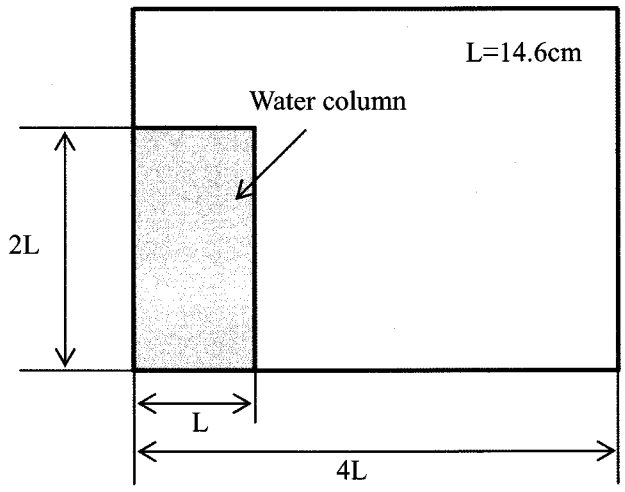

Figure 3.3: Initial geometry of a water column.

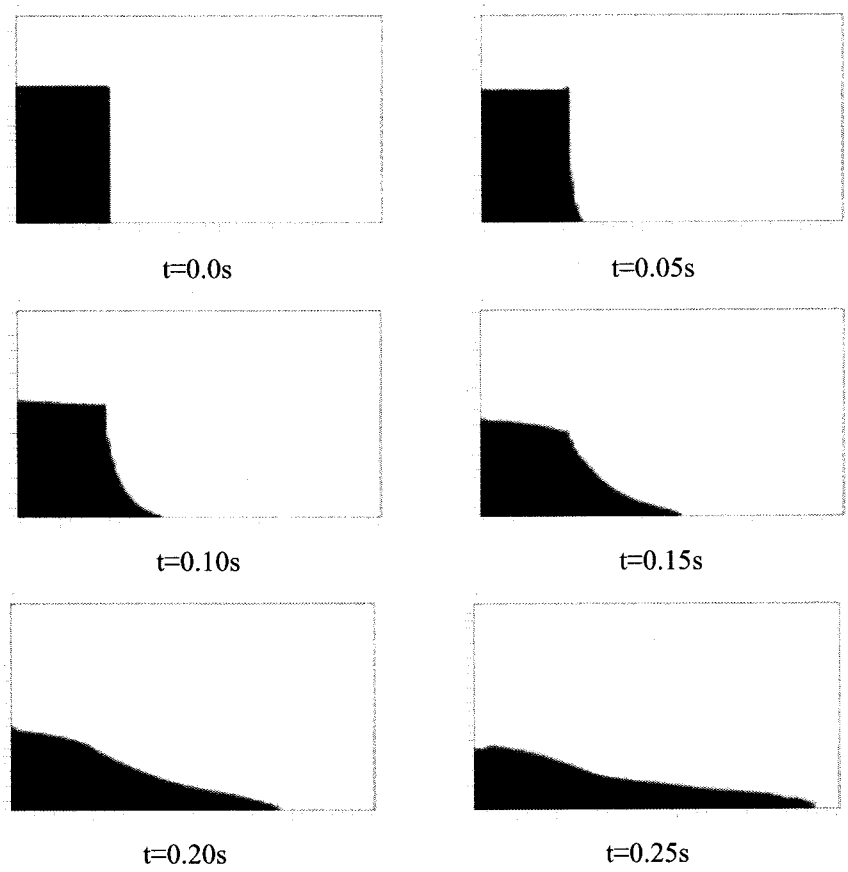

Figure 3.4: Fluid distributions obtained by the simulation of the broken dam problem at times 0.0s, 0.05s, 0.10s, 0.15s, 0.20s, and 0.25s. The free surface is defined by a counter line of $\phi = 0.5$.

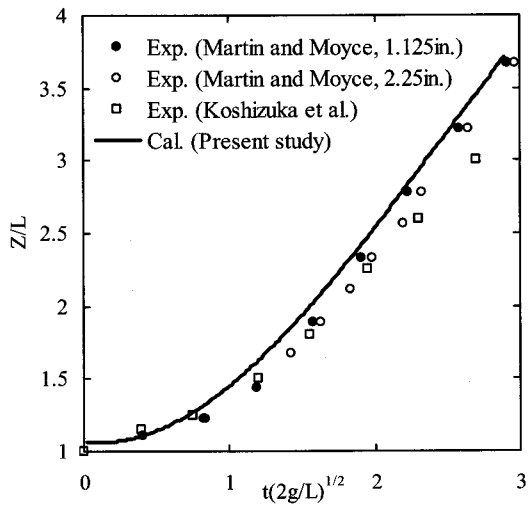

Figure 3.5: Motion of the leading edge in collapse of a water column.

3.3.2 Bubble Rising and its Interactions

In the two-phase flow simulations, it is important to accurately simulate the interaction between the air and the water. Thus, in this section, simulations of rising bubbles in a liquid are performed in order to validate whether the present method can accurately represent the interaction processes of the air bubbles and the water.

First, we consider a problem that air-bubbles rising in the surrounding water desorbed to the air through the interface. The initial air bubble radius is set to be 0.1m, and the pressure profile is assumed to be hydrostatic. The fluid is at rest initially. The viscosity coefficients and the fluid densities for the gas and the liquid are set to real values, such that μ_{gas} =1.8×10^{-5} Pa・s, $\mu_{liq.}$ =1.0×10^{-3} Pa・s, ρ_{gas} =1.2 kg/m^3, and $\rho_{liq.}$ =1.0×10^3 kg/m^3. Also, a realistic value of the surface tension coefficient σ =7.2×10^{-2} N/m is used. The grid number is 50×50, with the resolution of 0.02m×0.02m. The boundary conditions are free-slip at the walls. Figure 3.6 shows the time evolution of the air bubble. The air bubble rising in the water is deformed on the bottom side of the bubble. The largely deformed bubble is split and pushes up the water surface. Finally, the bubble is absorbed into the air. The water surface deformed by the bubble rising is pushed up largely through the surface tension. The observed behaviors of the bubble are similar to those found in the simulation by Sussman et al. [23] in the two-fluids case with a high density ratio.

Second, as the additional test problem, interaction of two bubbles with the same density is computed in a two dimensional system with gravity. When the two-phase flow simulation is performed in a high velocity regime, it is considered that a very complicated interaction between the gas and the water through the surface tension is taken place. Thus, it should be necessary to validate the capability of the present method to represent not only the single bubble interacting with the water, but also two bubbles interacting with each other. The initial radii of two bubbles are set to be 0.1m and 0.15m with distance of the centers of 0.30m. Other numerical conditions are as same as those of the previous numerical test problem. Figure 3.7 shows time evolutions of the two air bubbles, where one can see that the lower bubble moves faster. As the time advances, the lower bubble produces an upward jet. At time t=0.1, the head of the lower bubble almost cached up with the bottom of the upper bubble because the lower bubble speed is faster than the upper one due to the larger buoyancy force. At t=0.2, the two bubbles merge into a single one. At t=0.4, vortex motion created in the bottom part of the lower bubble results in a jet which penetrates into the stem of the merged bubble. The legs of the lower bubble are relatively straight and do not roll up as seen in the simulation by Chang et al. [57] without the surface tension. This is because the surface tension has an additional regularization effect near the region of large curvature. The behavior and the shape of the interacting two bubbles are similar to those of the simulation result by Chang et al. [57] in the two fluids case with a high density ratio. Therefore, it is confirmed that the present simulation method can be

applied to the gas-liquid interaction process through the surface tension even with complicated behaviors such as bubble deformation, splitting, and merging.

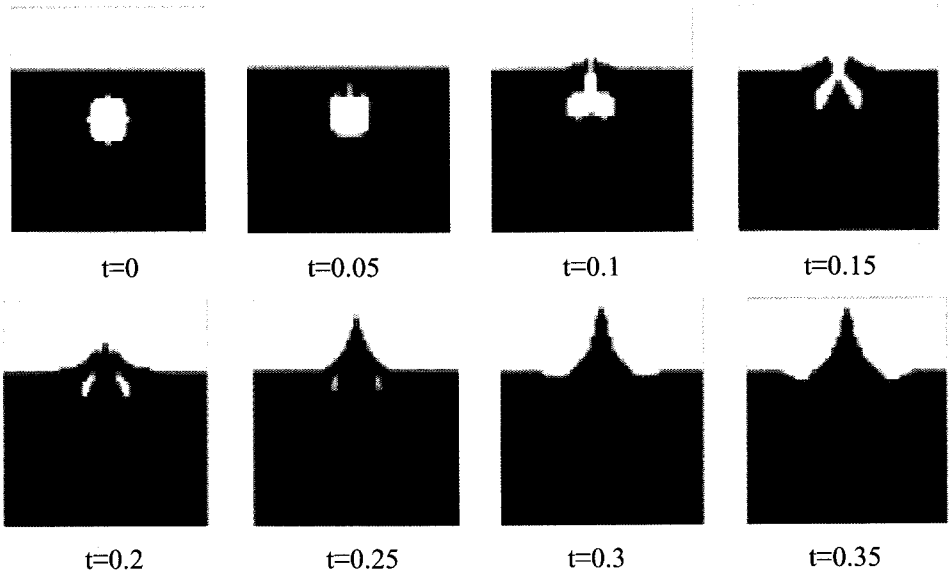

Figure 3.6: Behaviors of a rising bubble and its interaction with the water surface.

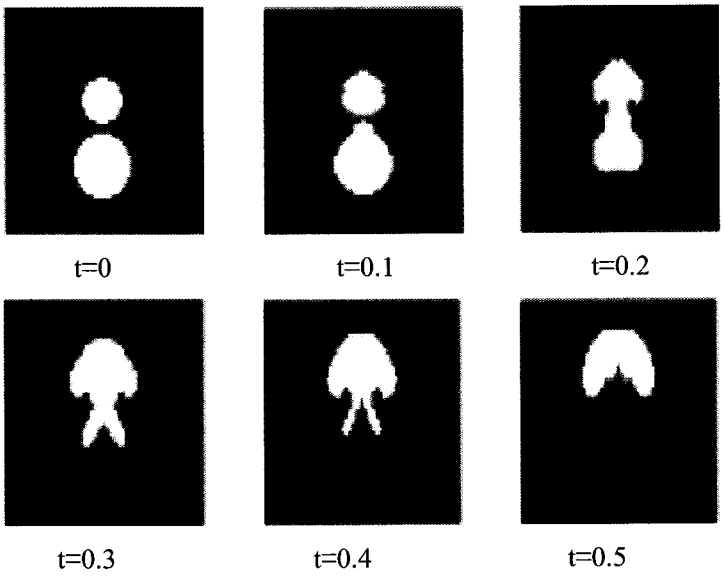

Figure 3.7: Behaviors of rising two bubbles and their interaction.

3.4 Numerical Procedure of Two-Phase Flow Simulations

3.4.1 Numerical Domain

In the present study, the two-phase flow simulations are started from the gas velocity field obtained from fully developed turbulence simulations of an open-channel gas flow with the

stationary water-phase. The turbulence in the gas-phase is driven by a constant pressure gradient in the streamwise direction. Hereafter, we call the first gas-phase and the second two-phase flow simulations Process 1 and 2, respectively.

The numerical domain used for the simulation in Process 1 is shown in Figure 3.7. The accuracy of C-CUP method will be checked in comparison with the conventional simulation with the spectral method. The fully turbulent fields obtained in Process 1 are used for the initial values of the two-phase flow simulations in Process 2.

In the Process 2, the two-phase flow simulations are performed in the numerical domain shown in Figure 3.8. Being based on the statistical analysis of the turbulence, we will discuss characteristics of the turbulence near a free-surface, and the momentum transfer process through the free-surface quantitatively.

The numerical domain similar to tank-experiments is employed so that the depth is consistent with that of the tank-experiments [7, 8]. In the both Processes 1 and 2, the numerical domains are $6.4\delta\times\delta\times3.2\delta$ or $6.4\delta\times1.5\delta\times3.2\delta$ in the unit of the vertical height δ. The x–, y–, and z–axes of the Cartesian coordinate system are defined in the streamwise, vertical, and spanwise directions, respectively.

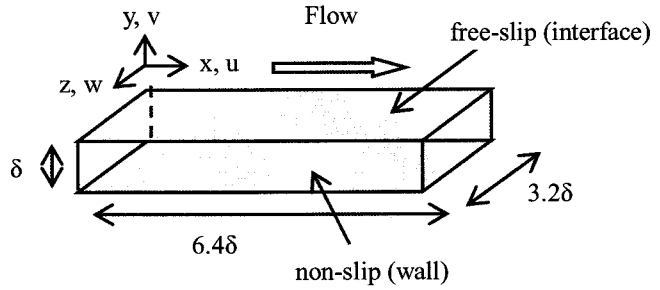

Figure 3.7: Numerical domain of open-channel flow simulations (Process 1).

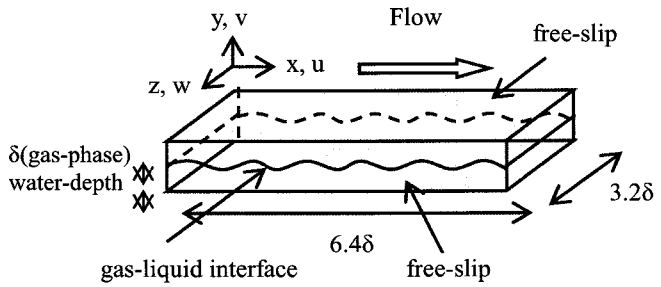

Figure 3.8: Numerical domain of two-phase flow simulations (Process 2). The water depth is set to be $0.5\,\delta$ and δ for the Case 1a, 2a, and Case 1b, 2b, respectively. Detailed definition is shown in the text.

3.4.2 Model Setting

In this study, the two-phase flow simulations for a gas and a liquid are performed with a numerical setting as given bellow. A grid system is staggered. Turbulent Reynolds number Re_τ, which is defined by the friction velocity u_* in the gas-phase, the gas kinematic viscosity ν and the vertical height δ, is chosen from 150 to 300 in order to investigate the wind velocity dependence of the friction. The corresponding spatial resolutions are set to $15\times0.6\times7.5\ \nu/u_*$ in all cases. An effect of the water depth on the evaluation of the friction velocity is also investigated. In the deeper cases denoted as Case 1b and Case2b, the water depth is consistent with that of the tank-experiments [7, 8]. The numerical parameters are listed in Table 3.2.

The wind velocity is in a regime that the free-surface deformation accompanied with ripples can not be ignored, and is comparable to the representative velocity in the tank-experiments. The representative wind velocity U_c in gas-phase is about 3.5m/s in the Cases 1a and 1b with Re_τ=150. The Reynolds number normalized by the streamwise mean velocity U_c and vertical height δ is about 2300 which is almost the same value as that in the work by Kunugi et al. [58]. In Cases 2a nad 2b with Re_τ=300, U_c is about 7.0m/s .

The present simulation code based on the C-CUP method is implemented with the following schemes in order to improve the numerical stability and accuracy in the high velocity range. The rational CIP method [38, 39] can avoid negative values of the density and pressure in the transition region near the free-surface. The tangent transformed density function [33], which defines the transition region, can reduce the numerical diffusion of the transition region and keep the compactness.

In Process 1, the periodic boundary condition is employed for the streamwise and spanwise directions, while the non-slip and the free-slip conditions are adopted to the bottom wall and the free-surface, respectively. The boundary conditions are as same as those in the previous simulations of open-channel flow. Perturbed velocity fields and the isothermal stratified states are given as the initial conditions. The computation is carried out till 15000 in the non-dimensional time units ($T^+ = u_*^2/\nu$) to obtain the fully developed turbulent velocity fields. After the turbulent flow reached a statistically steady state, the computation is continued further for T^+=1500, then, all statistical values are calculated by time and horizontal spatial averages.

In Process 2, the free-slip condition imposed on both of the bottom and top walls in order to prevent artificial turbulent energy production which may affect the momentum transfer process through the free-surface. The periodic boundary condition is used for other directions. The liquid-phase at T^+=0 is assumed to be stationary and in the isothermal stratified state. The initial free-surface is located at the mid-plane of total height.

Corresponding to the value of the fetch F=0.15 and 0.225m, the computations are carried out till T^+=75 or 150, respectively, where F represents for the blowing distance of the representative wind over the free-surface. The simulations are continued to T^+=150 for both cases of Re_τ=150 and 300. Then, the statistical analysis is done by time and horizontal spatial averages.

Table 3.2: Numerical conditions.

	Reynolds number: Re_τ	Fetch: F [m]	Grid number: $N_x \times N_y \times N_z$	Spatial resolution: $\Delta x^+ \times \Delta y^+ \times \Delta z^+$	Water depth	Time increment : Δt^+
Case 1a	150	0.15	64×256×64	15×0.6×7.5	0.5 δ	0.015
		0.225				
Case 1b		0.15	64×384×64	15×0.6×7.5	δ	0.015
		0.225				
Case 2a	300	0.15	128×512×128	15×0.6×7.5	0.5 δ	0.015
		0.225				
Case 2b		0.15	128×768×128	15×0.6×7.5	δ	0.015
		0.225				

4 Simulation Results for Open-Channel Turbulence

4.1 Verification of Accuracy

Results of the statistical analysis for the open-channel turbulence simulation (Process 1) are shown in Fig. 4.1 - 4.3 in order to verify accuracy of the present method. In each figure, the obtained results are compared with those of DNS for the closed-channel flow by Iwamoto et al. [59]. Their results for an incompressible flow given by the spectral method are in good agreement with experiments. They used 128×97×128 grid points of $Re_\tau = 150$ with spatial resolutions of Δx^+=18.4, Δy^+=0.08-4.91, and Δz^+=7.36. It is possible to compare our results for the open-channel turbulence with those of the closed-channel one because the turbulent statistics in the bulk region, except near the free-surface, are almost the same for both cases [16, 17, 60-62].

Figure 4.1 shows mean profiles of the streamwise velocity, where the velocity is normalized by the wall-shear velocity u_*, and the distance from the rigid wall y^+ is measured in the wall unit $y^+ = yu_*/\nu$. In all regions of both cases for Re=150 and Re=300, the present simulation results are in good agreement with those of the closed-channel flow. It is considered that a fully developed turbulent velocity fields are obtained because the log-law is satisfied at y^+>30.

Reynolds stress and total shear stress profiles are plotted in Fig. 4.2, where the Reynolds stress is normalized by the wall-shear velocity u_*. The Reynolds stress profiles are in good agreement with those of the simulation results with the spectral method. The almost linear profiles of the total shear stress also suggested the fully developed turbulence.

The profiles of the pressure-strain correlation rate Π_{ij} are presented in Fig. 4.3, where the $\Pi_{ij} = \overline{p'/\rho(\partial u'_j/\partial x_i + \partial u'_i/\partial x_j)}$ normalized by u_*^4/ν. In the two-phase flow simulation, the pressure-strain correlation rate represents the turbulent energy transfer from the gas to the liquid. The profiles, except near the top boundary, are also in good agreement with those of the spectral method.

The results given above demonstrate accuracy of the present simulation method for the open-channel flow. It would be, thus, appropriate that the velocity fields obtained here (Process 1) is applied to the initial conditions for two-phase flow simulations.

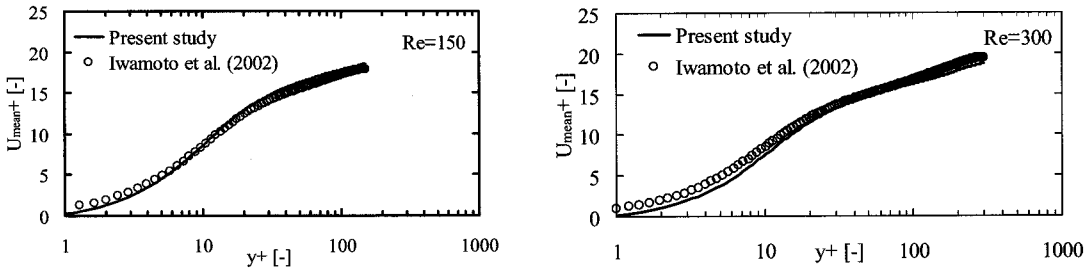

Figure 4.1: Streamwise mean velocity profile (left: Re=150, right: Re=300).

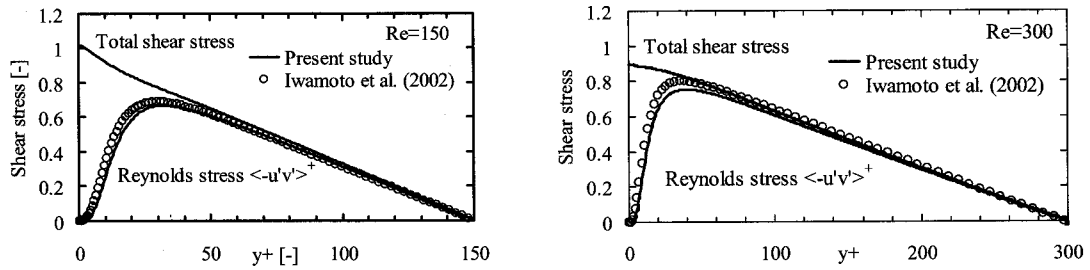

Figure 4.2: Profiles of Reynolds stress and total shear stress (left: Re=150, right: Re=300).

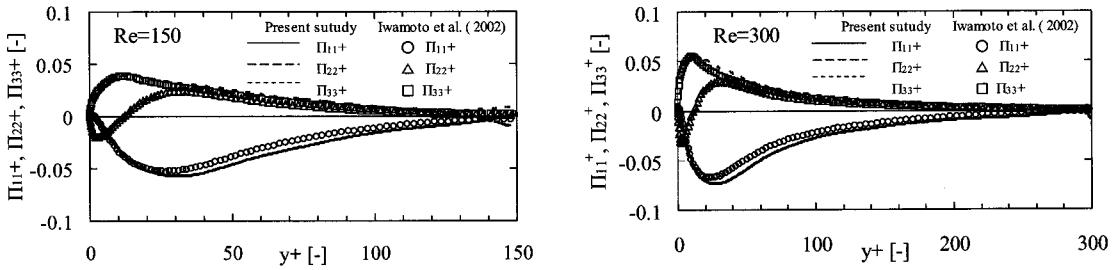

Figure 4.3: Profiles of pressure-strain correlation (left: Re=150, right: Re=300).

4.2 Comparison with Conventional Simulations of Closed-Channel Flow

In our open-channel flow simulations, the free-slip condition is imposed on the top boundary (free-surface) which is assumed to be flat in a case with the weak shear stress. Consistency of the present method is checked by comparing the results of the present calculations with those of the conventional DNS [16]. In each figure shown below, the spectral simulation results of the closed-channel flow by Iwamoto et al. [59] are also plotted along with ours.

Figure 4.4 shows vertical profiles of the turbulent intensity near the top boundary, where the root-mean-square (rms) velocity is normalized by the wall-shear velocity u_*. Near the free-surface region (y^+>140 for Re=150, and y^+>280 for Re=300) , vertical velocity fluctuations $v_{rms}{}^+$ are damped

to be zero due to the presence of the top boundary, while spanwise fluctuations w_{rms}^{+} are increased. These are different from the results of the closed-channel flow simulations. The local minimum of the spanwise component is found farther from the top boundary than the streamwise one, which is consistent with the previous simulation [17] as well as the experiment [7]. These behaviors are also consistent with the explanation from the previous studies [7, 17, 61, 62] such that the normal turbulent kinetic energy is redistributed mainly into the spanwise component through the pressure-strain correlation terms due to the presence of the top boundary with the free-slip conditions. Perot and Moin [63] reported that the turbulent energy redistribution is controlled by the splat which is a structure of the vertical motion caused by the pressure-strain correlation terms near the top boundary.

To verify the transfer mechanism mentioned above, Fig. 4.5 shows profiles of the pressure-strain correlation near the top boundary. The vertical component Π_{22}^{+} rapidly decreases just below the top boundary and changes from positive to negative, whereas the spanwise component Π_{33}^{+} remains positive and increases near the top boundary. The obtained result is also consistent with the previous ones [17, 61], and can explain the behavior seen in Fig. 4.4 such that the vertical component of the turbulent intensity decreases but the spanwise one increases near the top boundary.

Figure 4.6 shows profiles of the rms of vorticity fluctuations near the top boundary. Only the normal component of the vorticity fluctuations appears near the top boundary. This means that the fluctuations of the velocity normal to the free-surface are substantially smaller than those in the horizontal directions, and that the fluid motion near the top boundary is quasi-two-dimensional [64].

The above results indicate that the present calculations with the C-CUP method can give consistent results with the previous open-channel flow simulations, and that the top boundary can be treated as flat because the turbulent statistics in the bulk region are not seriously affected by the type of the top boundary for the very weak shear stress.

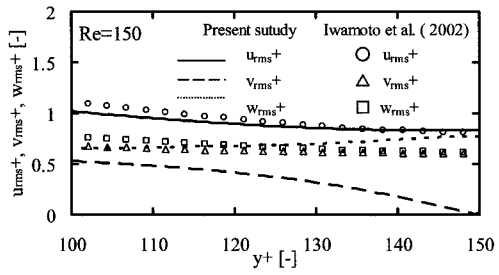

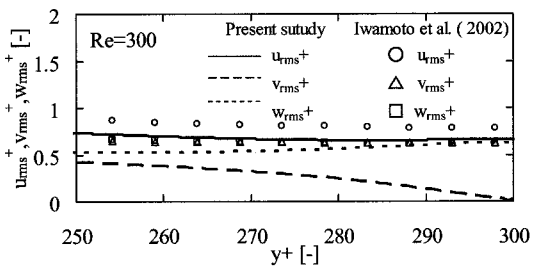

(a) Re=150 (Top boundary position: y^+=150) (b) Re=300 (Top boundary position: y^+=300)

Figure **4.4**: Profiles of the turbulent intensity near the free-surface.

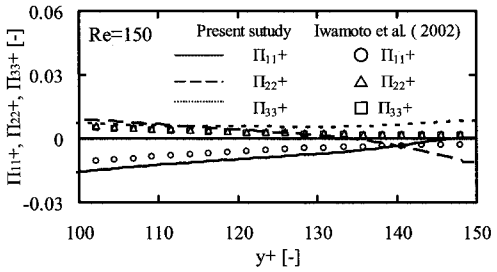

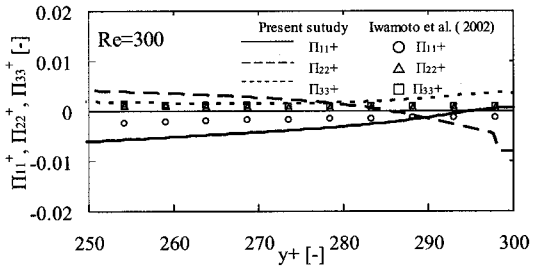

(a) Re=150 (Top boundary position: y^+=150) (b) Re=300 (Top boundary position: y^+=300)

Figure **4.5**: Profiles of the pressure-strain correlation profiles near the free-surface.

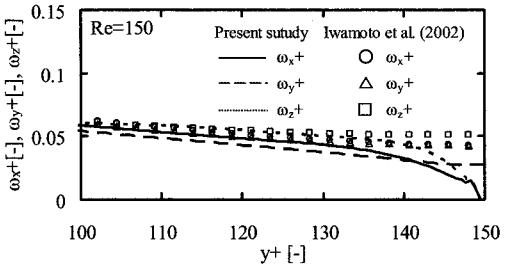

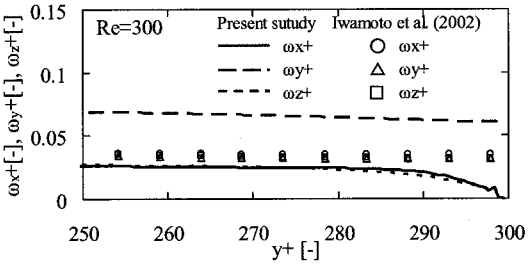

(a) Re=150 (Top boundary position: y^+=150) (b) Re=300 (Top boundary position: y^+=300)

Figure **4.6**: Profiles of the root-mean-square of the vorticity fluctuation profiles near the free-surface.

5 Simulation Results for Two-Phase Flows

5.1 Statistical Analysis of Turbulence near the Free-Surface

In this section, we will make statistical analysis of the simulation results of the two-phase (gas-liquid) flow with the deformable interface (free-surface). The initial position of the free-surface is $y^+=75$ ($y^+=150$) for Re=150 (Re=300). Vertical profiles of fluctuations of the density function, which defines the free-surface position in the steady turbulence, are shown in Figure 5.1. It can be seen that the free-surface fluctuations are increased as the fetch F increases for all cases. The magnitude of the free-surface fluctuations with the fetch F =0.225m are about 0.20mm, 0.20mm, 0.25mm, and 0.25mm for Case 1a, Case1b, Case2a, and Case2b, respectively, and are larger than the experimental result of about 0.05mm by Komori, et al. [65]. They concluded that the DNS which treats the free-surface as a rigid slip wall is not appropriate for application to their experiments, not to mention a case with larger disturbance. Thus, since the magnitude of the free-surface fluctuations is about 5times larger than those of the experiment, it is necessary to simulate the free-surface explicitly.

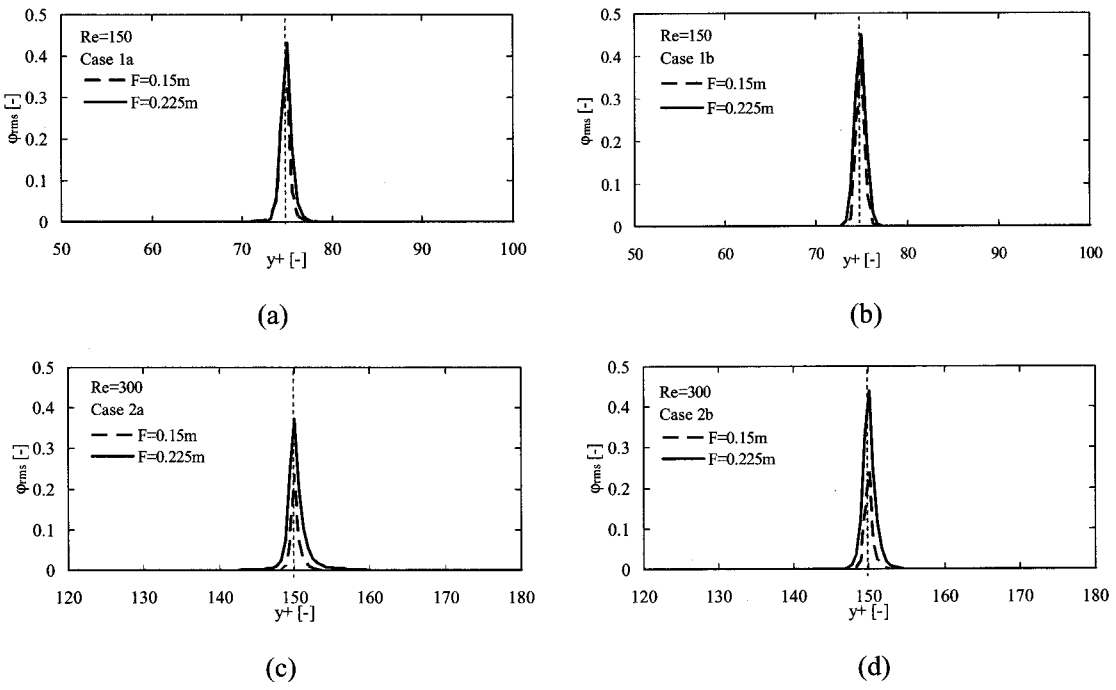

Figure **5.1**: Profiles of the root-mean-square of the density function fluctuation (doted line indicates the initial free-surface position).
(a) Case 1a (Re=150, Water depth: 0.5 δ); (b) Case 1b (Re=150, Water depth: δ);
(c) Case 2a (Re=300, Water depth: 0.5 δ); (d) Case2b (Re=300, Water depth: δ)

Profiles of the root-mean-square of velocity fluctuations are shown in Figure 5.2. In all cases, the streamwise velocity u_{rms}^{+} is remarkable. The vertical velocity component v_{rms}^{+} normal to the free-surface is induced near at the free-surface even in the liquid side. Moreover, the all components of the velocity fluctuation in gas-phase decrease as the fetch F increases as shown left figures for a whole region, while the vertical velocity v_{rms}^{+} near at the free-surface in the liquid side increases as shown in the right figures. These results indicate that the turbulent energy in the gas-phase is transported to the liquid-phase through the fluctuating free-surface because the initial velocities in the liquid-side are zero in all cases. This is also reported by Kunugi et al. [31, 32] using MARS. Therefore, it is necessary to take into account the effect of the free-surface deformation for studying transport of the physical quantities between the gas- and liquid-phase, when a large shear stress is given on the free-surface as considered in this study.

We shall discus that the reasons for the increase of vertical velocity fluctuations near the free-surface. Previous studies [17, 61, 63] for the open-channel flow with no deformation of the free-surface in the liquid-phase explained the redistribution of turbulent energy such that the vertical velocity fluctuation decreases but the spanwise one increases near the free-surface. This is because the surface-normal component of the pressure-strain correlation term decreases and becomes negative near at the free-surface boundary, while the spanwise one increases and has a positive value. Figure 5.3 shows that the pressure-strain correlation term peaks near at the free-surface. The increase of the turbulent intensities near the free-surface in liquid-side shown Fig. 5.2 means the production of the turbulent energy through the fluctuation of the free-surface excited by shear stress of gas flow. As the results, the turbulent energy is transferred to the liquid-phase. In the Case 2a and 2b for Re=300, the pressure-strain correlation terms are larger than that of the Case 1a and 1b for Re=150 not only near at the free-surface but also in the gas-phase. In the cases of Re=300, the interaction between the gas- and liquid-phases through the free-surface is stronger than that for Re=150, since the wind speed is higher. This results in the stronger turbulent production near at the free-surface in the gas-phase. Near the free-surface in the liquid-side as shown in the right figures, it can be seen that the streamwise component Π_{11}^{+} is negative near at the free-surface, while the surface-normal component of the pressure-strain correlation term Π_{22}^{+} have a positive values greater than spanwise component Π_{33}^{+}. However, it can be seen that there is difference between the Case 1a (2a) and Case 1b (2b). It is considered that the difference is caused by the difference of the numerical condition of the water depth. In Case 1a and Case2a, with the smaller water depth the evaluation of the pressure-strain correlation term near at the free-surface is considered to suffer from the effect of the pressure fluctuation excited at the bottom of the water. Nevertheless, the behavior of the turbulent energy transfer to the liquid-phase, as well as the variation of the sign of each component, is similar among all cases. Therefore, in cases that the free-surface deformation effect cannot be ignored, it is

suggested that the dominant energy is transferred from the streamwise component, which has main turbulent energy, to the surface-normal component via pressure-strain correlation term. This behavior is consistent with the vertical component of the turbulent intensities which increases near at the free-surface in the liquid-phase as shown in Figure 5.2.

In the previous studies [64], which focused on the open-channel flows only in the liquid-phase with no deformation of the free-surface, only the normal component of vorticity can be finite at the interface. The result indicates that the fluid motion near at the free-surface is quasi-two-dimensional. In this study, where the free-surface fluctuation cannot be ignored as shown in Fig. 5.4, presence of three-dimensional turbulent structures is suggested because there appears not only the vorticity normal to the free-surface, but also other components. Since the spanwise component of the vorticity ω_z^+ is dominant and the gas density is much less than the liquid one, the turbulent structures near the free-surface are resemble with those in the wall turbulences. Moreover, the spanwaise component of the vorticity ω_z^+ appears also in the liquid-phase near at the free-surface. Therefore, it is suggested that the vertical turbulent mixing occurs due to the vertical velocity fluctuation accompanied with the spanwise component of the vorticity, which can be treated by solving the free-surface fluctuations explicitly. According to the analysis in Fig. 5.4, difference in the profiles of the vorticity fluctuations between each case are negligible.

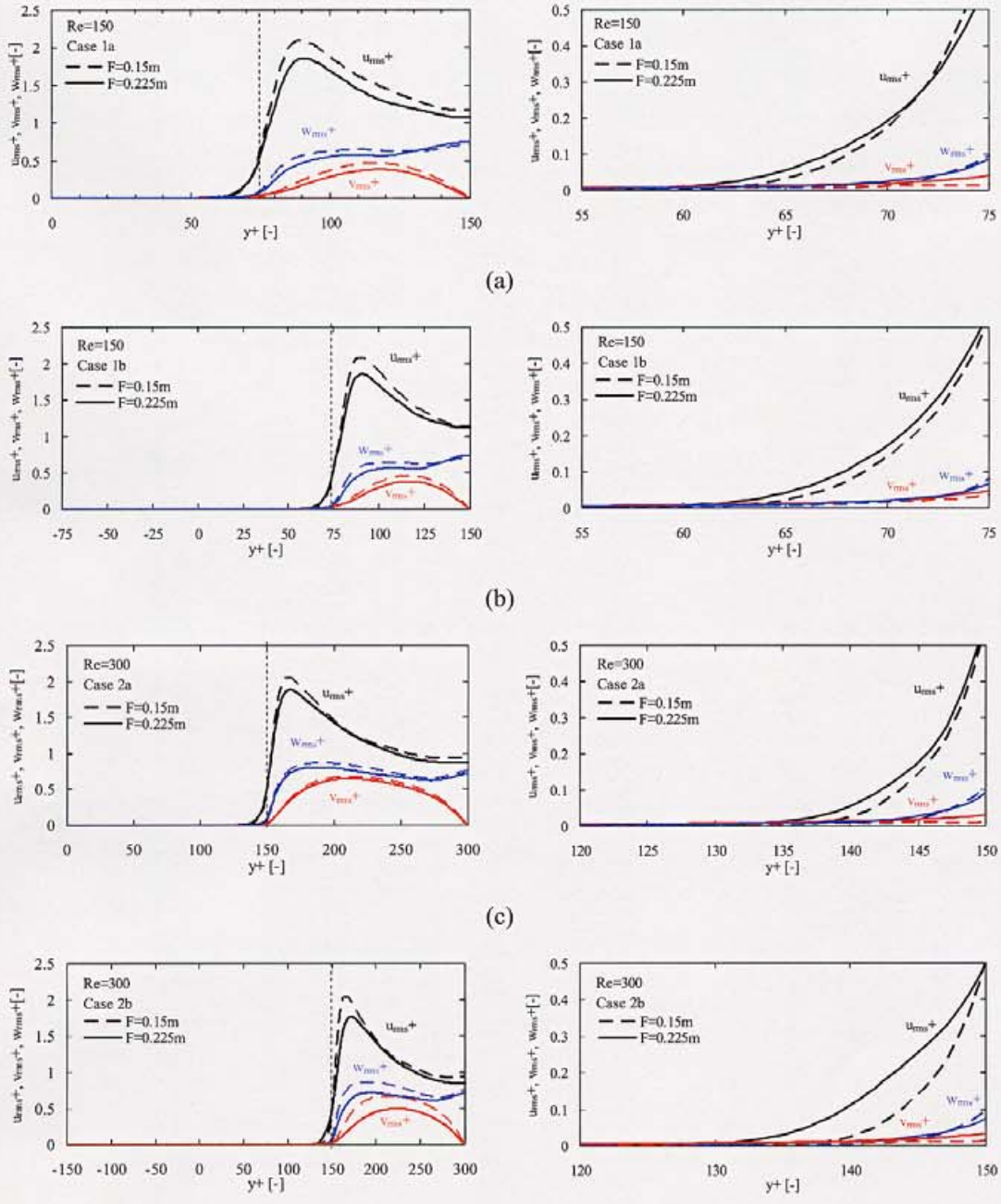

Figure **5.2**: Profiles of the root-mean-square of velocity fluctuations. The left figure shows a whole, but only a part of the system near at the free-surface in the liquid side is presented in the right panel (doted line indicates the initial free-surface position).

(a) Case 1a (Re=150, Water depth: 0.5 δ); (b) Case 1b (Re=150, Water depth: δ);

(c) Case 2a (Re=300, Water depth: 0.5 δ); (d) Case2b (Re=300, Water depth: δ)

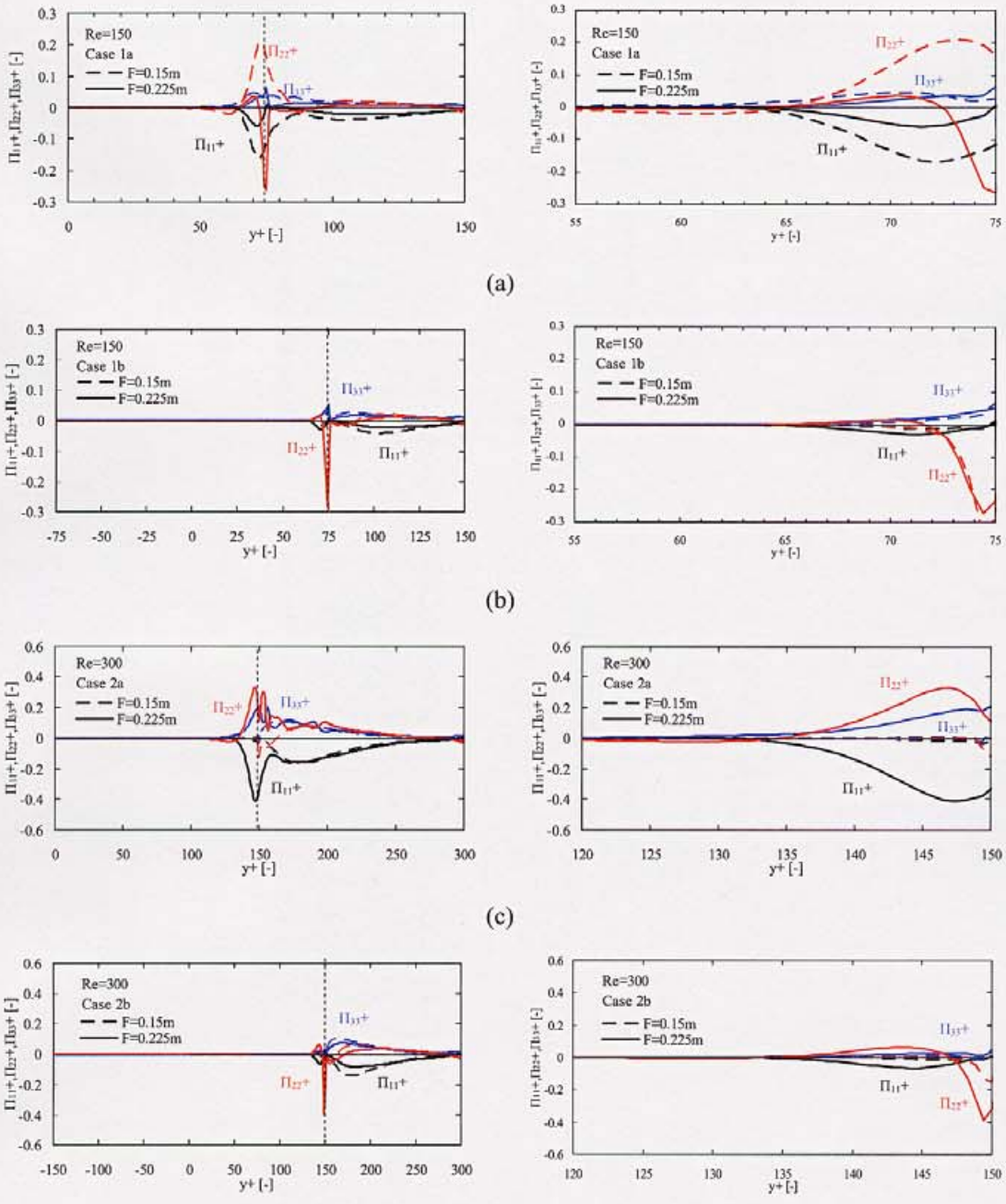

Figure **5.3**: Profiles of the pressure-strain correlation terms. The left figure shows a whole, but only a part of the system near at the free-surface in the liquid side is presented in the right panel (doted line indicates the initial free-surface position).

(a) Case 1a (Re=150, Water depth: 0.5 δ); (b) Case 1b (Re=150, Water depth: δ);

(c) Case 2a (Re=300, Water depth: 0.5 δ); (d) Case2b (Re=300, Water depth: δ)

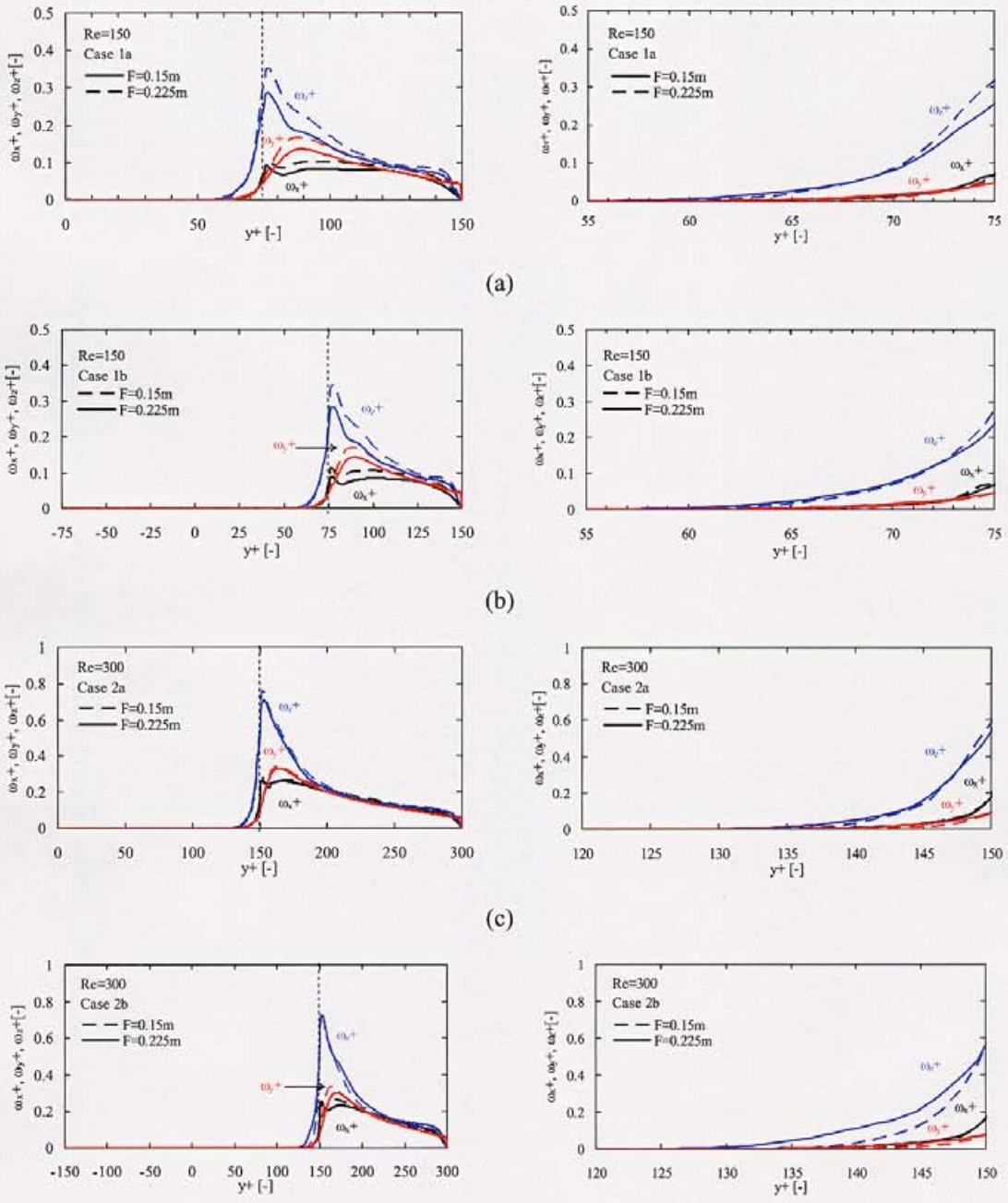

Figure **5.4**: Vorticity fluctuation profiles. The left and right Figures show all regions and near at the free-surface in the liquid side, respectively (doted line indicates the initial free-surface position).

(a) Case 1a (Re=150, Water depth: 0.5 δ); (b) Case 1b (Re=150, Water depth: δ);

(c) Case 2a (Re=300, Water depth: 0.5 δ); (d) Case2b (Re=300, Water depth: δ)

5.2 Relation between Reynolds Stress and Free-Surface Structure

Figure 5.5 shows the instantaneous distributions of the density function (left figures) and the Reynolds stress (right figures) at the initial free-surface level of y+=75, which are plotted with a time interval of T^+=20 from T^+=120 to 200 for Case 1b. In Fig. 5.6, the same plots as those in Fig. 5.5 are given for Case 2b. In figures of the density function, the black area represents the liquid-phase while the white area means the gas-phase. The instantaneous distributions of the density function reflect the free-surface structures. It can be seen that the turbulent structures are constituted of many ripples and small waves, which are developing with a time advance. The turbulent structures are also seen in the simulation by Kunugi et al. [32] with the MARS method as well as in the experiment by Ebuchi et al. [66] where the representative wind velocity is almost the same as that of the present study. By comparing the interface structure with the instantaneous distributions of the Reynolds stress at the free-surface level, there seems to be a correlation between them. This result suggests that the momentum transport process depends on the Reynolds stress near at the free-surface produced by the vertical velocity fluctuations in association with the free-surface fluctuation. In order to investigate the momentum transport process, it is necessary to investigate the relation between the Reynolds stress and the free-surface distribution more in detail, in terms of the statistical analysis.

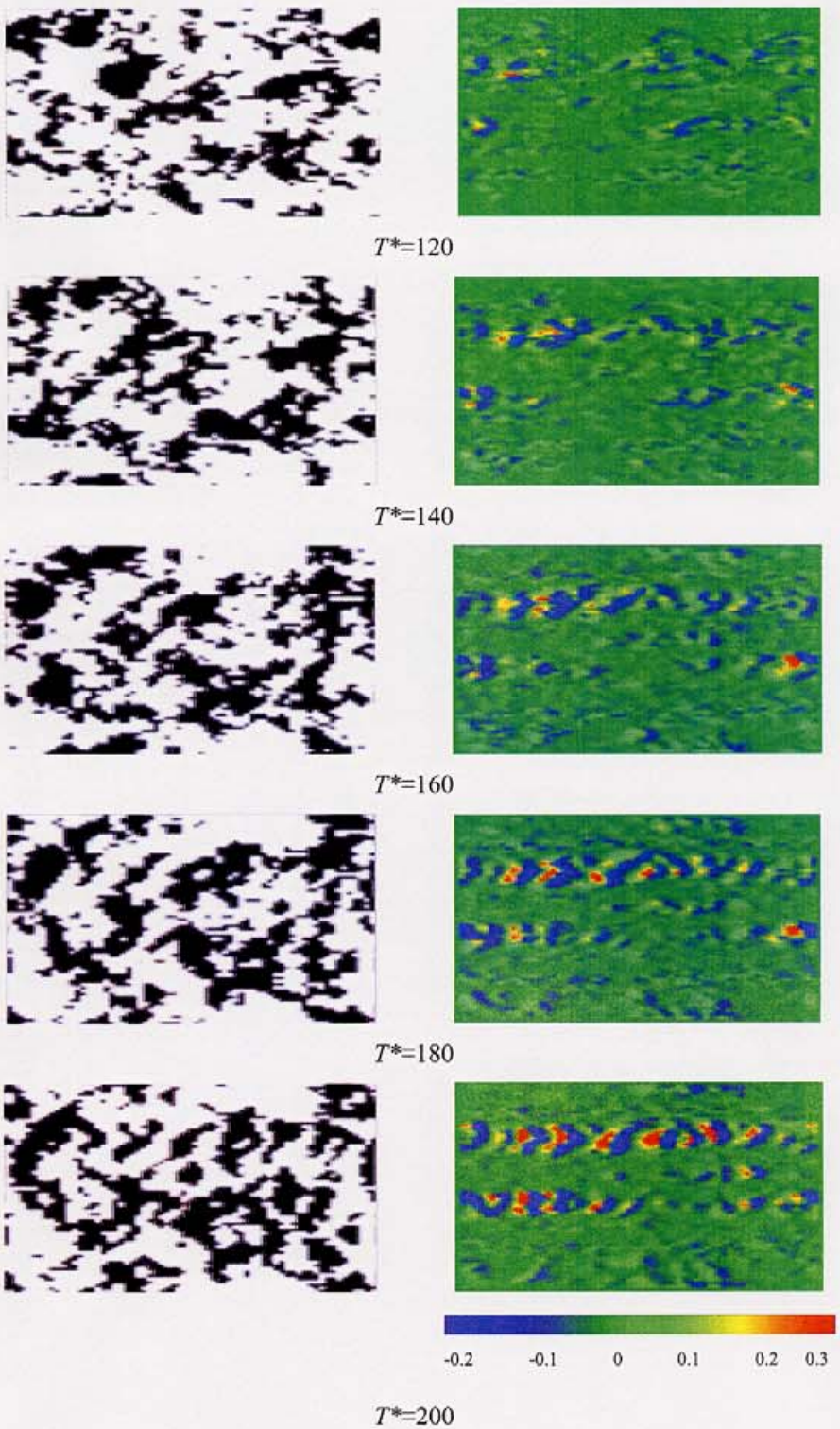

Figure **5.5**: Instantaneous distributions (a) density function ; (b) Reynolds stress at the averaged free-surface level (y+=75) in case of Case 1b. (Re=150, Water depth: δ)

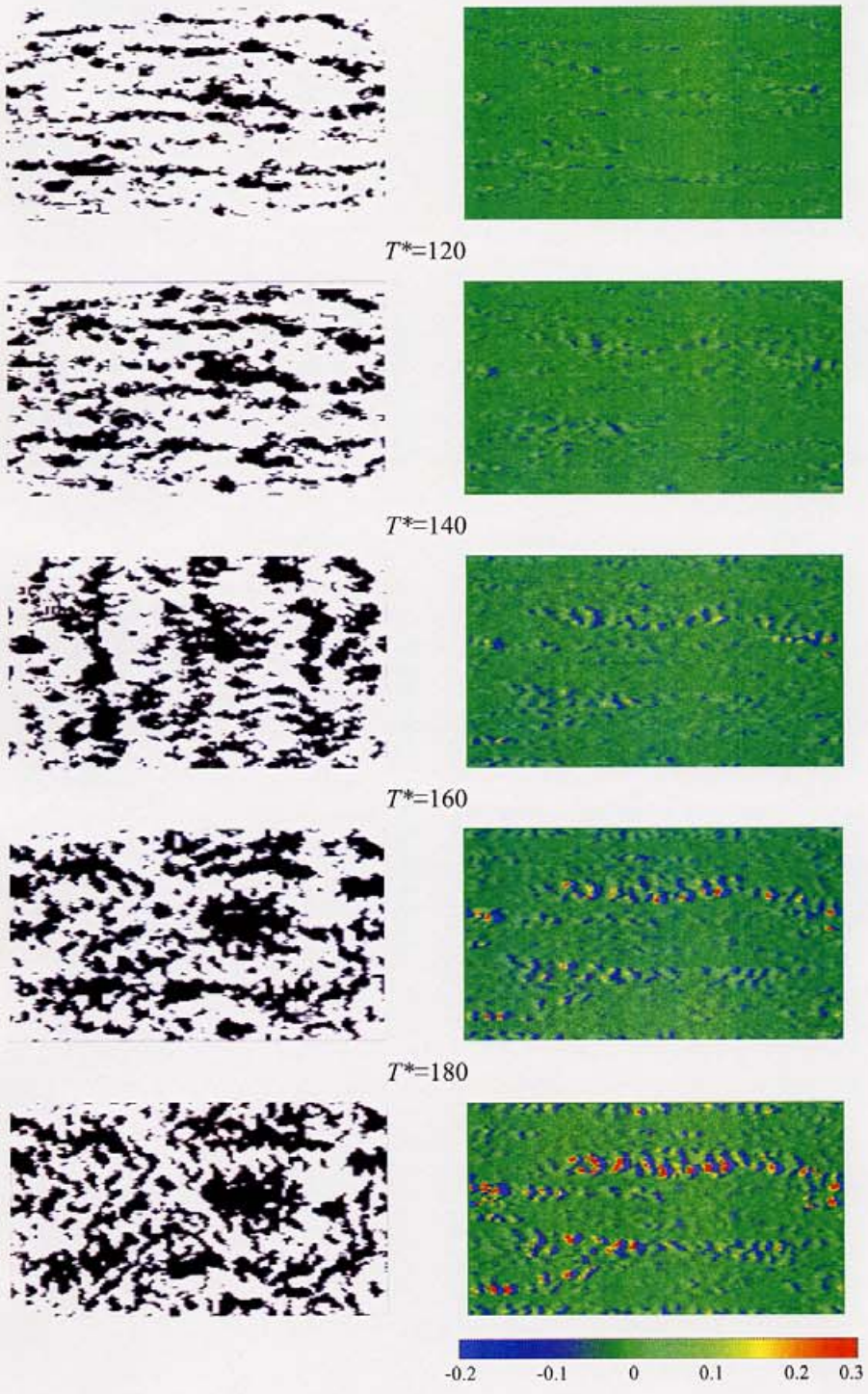

Figure **5.6**: Instantaneous distributions (a) density function ; (b) Reynolds stress at the averaged free-surface level ($y+$=150) in case of Case 2b. (Re=300, Water depth: δ)

We have investigated a relation between the Reynolds stress near at the free-surface in the gas-phase and the free-surface positions. Figure 5.7 shows five analysis points, which are denoted by (a) to (e). Figures 5.8 and 5.9 show time series of the Reynolds stress and the free-surface positions at each five point for Case 1b and Case 2b, respectively. It can be seen that the large positive spikes marked by arrows in the plots of the Reynolds stress, which indicate the downward momentum transfer, often appear at positions close to the crest of the wind-waves with relatively large wave height. In the experiments by Kawamura and Toba [67], it is shown that the Reynolds stress is produced in correspondence with 'burst' and 'sweep'. The former is the ascending low-speed air mass in back of the crest, while the latter is the descending high-speed air mass in front of the crest.

In order to statistically confirm the relation between location of the Reynolds stress production and a phase of the free-surface, an event histogram of the bursts of the Reynolds stress is plotted versus the wind-wave phase in Fig. 5.10, where all analysis points are used. Major events of the Reynolds stress are defined by the relation of $-u'v' = 10 \times \overline{-u'v'}$ as well as the experimental analysis done by Kawamura and Toba [67], and then, the positions are compared with the corresponding wind-wave phase. It can be seen that the burst positions are close to the crest over the windward side, as reported in the experiment by Kawamura and Toba [67]. The bursting phenomena over wind-waves account for a major portion of the Reynolds stress in the lower logarithmic boundary layer, as same as in the case over a flat plane. However, their occurrence has a close relation to the underlying wind-waves. It is shown in Fig. 5.10 that the separated shear layer over waves reattaches to the preceding wave surface at about $\theta = 260^{o}$. Therefore, the position of the shear stress spike is close to the crest over the windward side due to the reattachment. Okuda [68] has shown that a distinct high-vorticity region near the wave crest, which is associated with the shear stress spike just upstream of the crest, grows and attenuates while the wave is traveling. When air-flow separation begins, the shear stress may start to form the high-vorticity region and thicken with time. Okuda [69] studied this process numerically. However, it is suggested that dynamical interaction mechanisms between the air and wind-waves need to be dealt with as a time-dependent problem. In this study, by means of two-phase flow simulations with time-dependent equations, it is shown that the high-vorticity region is created near at the free-surface. In addition, the larger spikes of the Reynolds stress are observed in vicinity to the crest over the windward side. Therefore, it is considered that the process of an air-flow separation and the reattachment on the wind-waves associated with the momentum transport is accurately represented in the present simulations of the two-phase flow.

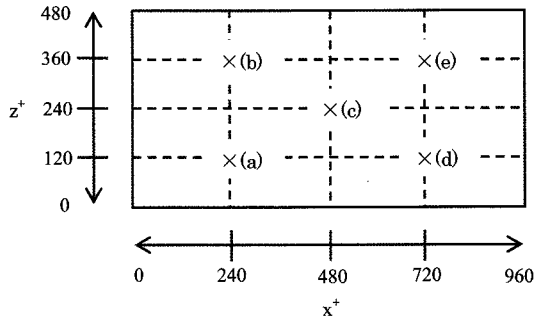

Figure **5.7:** Distributions of analysis points.

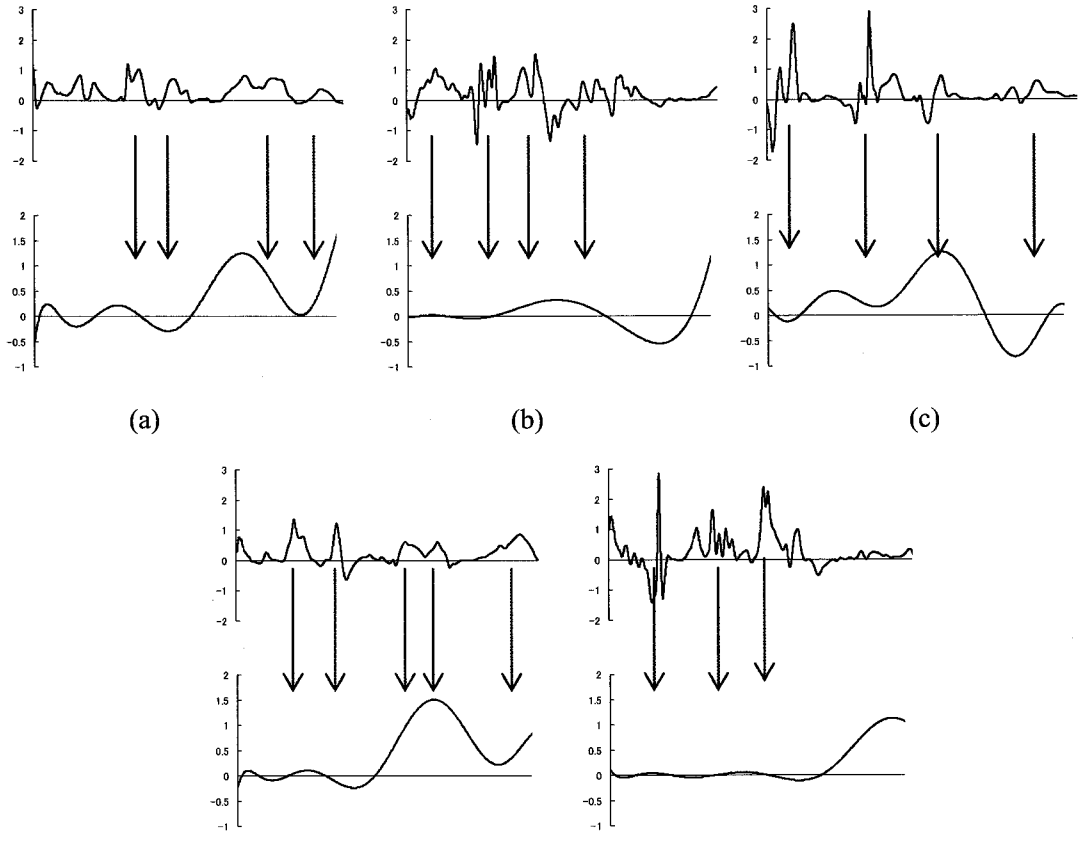

Figure **5.8:** Time series of Reynolds stress near the free-surface (y^+=84) in the gas-phase (upper figure) and the free-surface positions (lower figure) in Case 1b. Nondimensional units are used in each figure. The time goes from left to right.

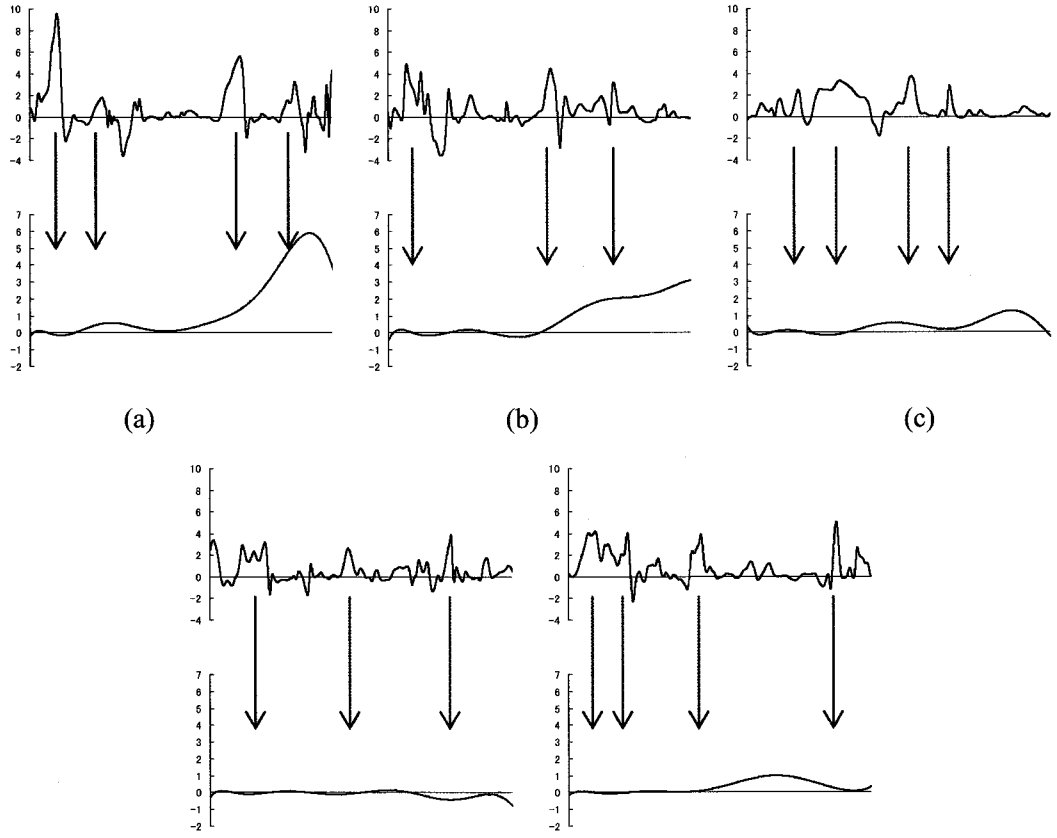

Figure **5.9:** Time series of Reynolds stress near the free-surface (y^+=169) in the gas-phase (upper figure) and the free-surface positions (lower figure) in Case 2b. Nondimensional units are used in each figure. The time goes from left to right.

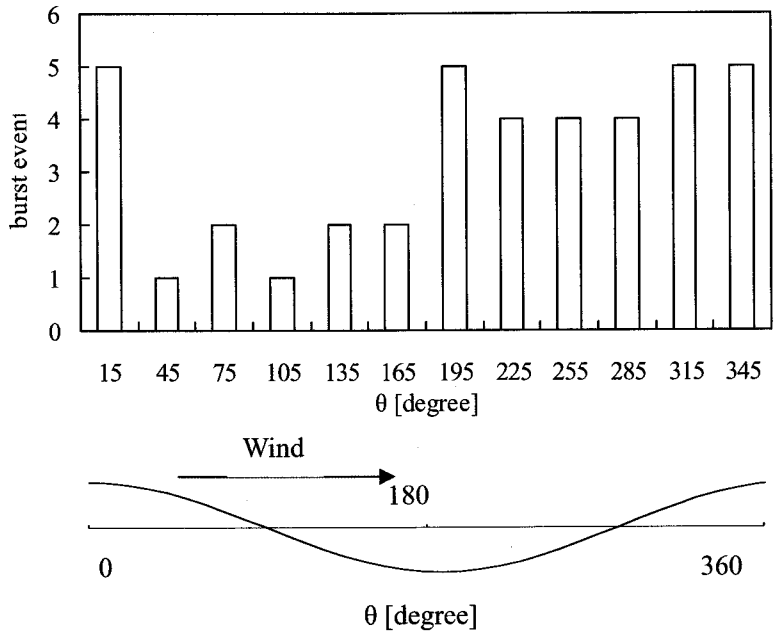

Figure **5.10:** Histogram of burst events of the Reynolds stress production versus the wind-wave phase.

5.3 Quantitative Evaluation of Friction Velocity

The momentum transferred through the free-surface is evaluated quantitatively in this section. Figure 5.11 shows the vertical profiles of the friction stress τ defined by $\tau = -\overline{u'v'}$ where u' and v' mean the steamwise velocity fluctuation and the vertical one, respectively. It can be seen that the friction stress for the Case 1a and Case2a, where the water depth of the numerical condition is smaller, is larger than that of the Case 1b and Case 2b, where the water depth is consistent with that of the tank-experiments [7, 8]. It is considered that the overestimate for the Case 1a and Case2a is caused by the effect of the pressure fluctuation excited at the bottom of the water. The pressure fluctuation may affect on the momentum transport process at the free-surface. As mentioned in Section 5.2, the bursting phenomena over wind-waves account for a major portion of the Reynolds stress. The position of the shear stress spike is also close to the crest on the windward side due to the reattachment. The air-flow reattachment results in the asymmetrical profile of the pressure rise along the wind-waves, and feeds turbulent energy into wind-waves. Thus, it is considered that the pressure fluctuation exited at the bottom of the water affects the momentum transfer process in the Cases 1a and 2a, and the evaluation of the friction stress is not sufficiently accurate. According to the above consideration, the Case 1b and Case 2b, where the water depth is consistent with that of the tank-experiments [7, 8] is considered appropriate to accurate evaluation of the momentum transport.

By using the friction stress τ presented in Fig. 5.11, the friction velocity u_* is calculated from the peak value of τ near at the free-surface in liquid-phase, such as

$$u_* = \sqrt{\frac{\tau}{\rho}}. \tag{5.1}$$

The evaluation method of u_* is also used in the experiment by Yoshikawa et al. [70]. The representative wind velocity U_c is estimated from the mean profiles of the streamwise gas-flow velocity which are shown in Fig. 5.12. The obtained values are summarized in Table 5.1.

The present results on the relation between the mean velocity in the gas side and the friction velocity is shown in Fig. 5.13 along with the tank-experimental data [15, 67, 70-74]. The simulation results are in good agreement with the tank-experimental data for both cases of the Reynolds numbers of 150 and 300. A better agreement is also found in the Cases 1b and 2b where the water depth is consistent with that of the tank-experiments [7, 8]. In the velocity range considered here, the free-surface deformation can not be ignored in contrast to the conditions for the conventional DNS studies, in which the liquid turbulence is decoupled from gas dynamics by supposing a flat interface and applying the free-slip condition. The plotted experimental data by Rashidi et al. [74] with very small values of U_c and u_* is in such condition, where the flat interface approximation is valid. Therefore, it is concluded that the present study shows the first quantitative evaluation of the friction stresses on the free-surface with large shear stress, and that the validity is confirmed by a comparison with the tank experimental data.

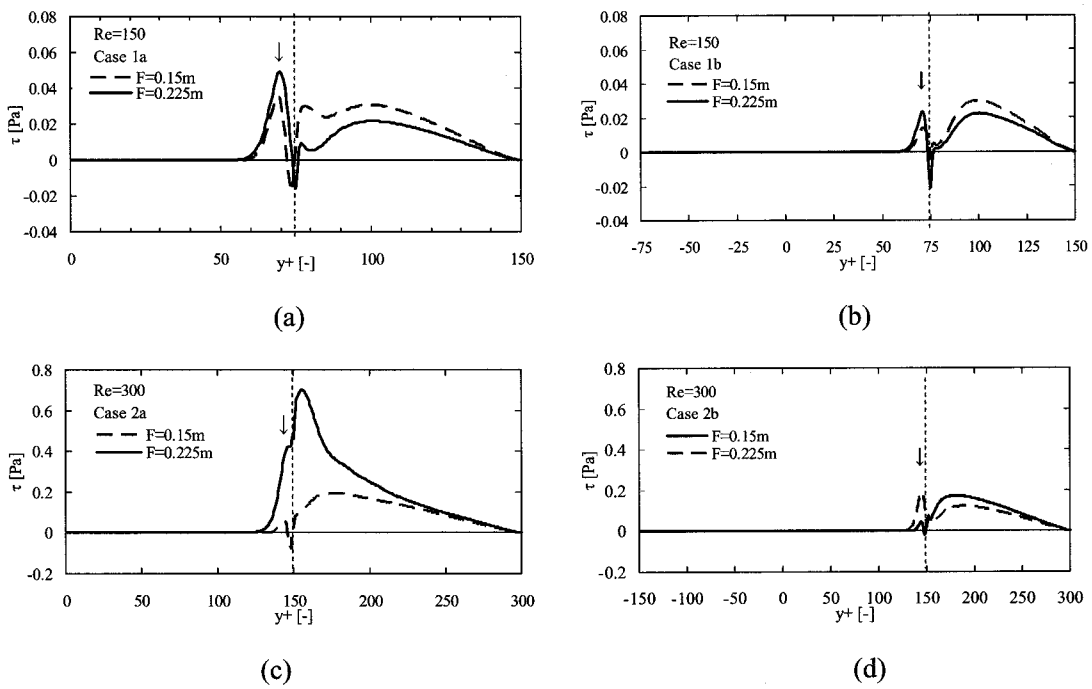

Figure **5.11**: Profiles of the friction stress (doted line indicates the initial free-surface position). (a) Case 1a (Re=150, Water depth: 0.5 δ); (b) Case 1b (Re=150, Water depth: δ); (c) Case 2a (Re=300, Water depth: 0.5 δ); (d) Case2b (Re=300, Water depth: δ)

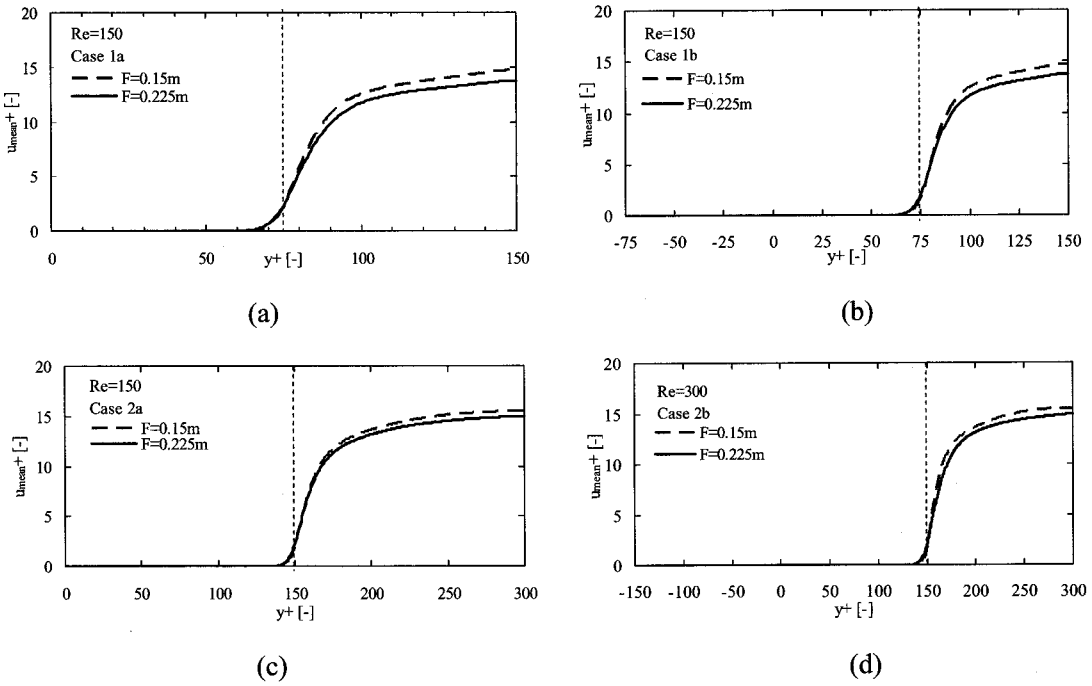

Figure **5.12**: Mean profiles of the streamwise velocity (doted line indicates the initial free-surface position).

(a) Case 1a (Re=150, Water depth: 0.5 δ); (b) Case 1b (Re=150, Water depth: δ);

(c) Case 2a (Re=300, Water depth: 0.5 δ); (d) Case2b (Re=300, Water depth: δ)

Table **5.1**: Relation between the friction stress at the free-surface, the rms value of the free-surface fluctuations and the mean gas-velocity.

	Re	Water depth	F [m]	U_c [m/s]	u_* [m/s]
Case 1a	150	0.5 δ	0.15	3.3	0.16
			0.225	3.1	0.19
Case 1b		δ	0.15	3.3	0.099
			0.225	3.1	0.13
Case 2a	300	0.5 δ	0.15	7.0	0.21
			0.225	6.8	0.54
Case 2b		δ	0.15	7.0	0.18
			0.225	6.7	0.36

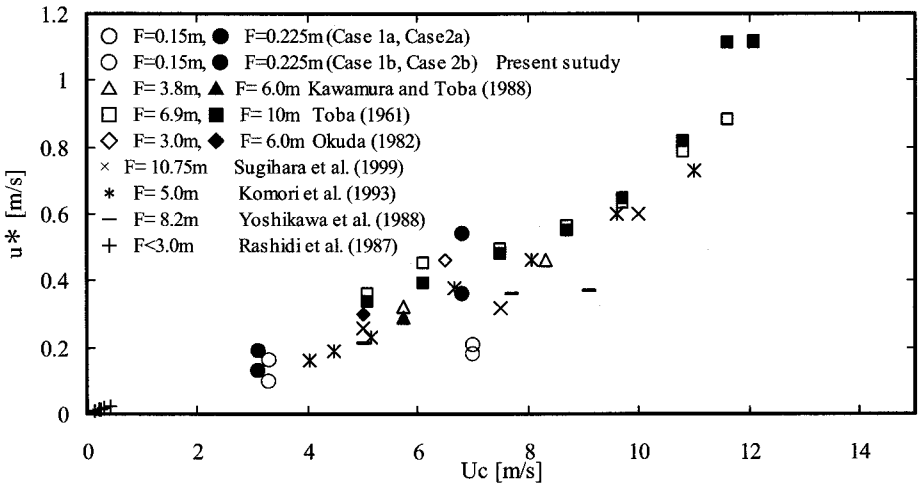

Figure **5.13**: Relation between the mean velocity U_c and the friction velocity u_* (where F means the fetch) The plotted experimental data are reported by; Kawamura and Toba [67], Toba [71], Okuda [72], Sugihara et al. [73], Komori et al. [15], Yoshikawa et al. [70], and Rashidi et al. [74], respectively.

5.4 Three-Second Power Law and Spectral Form for Growing Wind Waves

To compare the evaluated wind wave height with those obtained by tank-experiments and field observations, it is necessary to transform the magnitude of the free-surface fluctuation η_{rms} to the significant wave height Hs, which is defined as Hs=1.6η_{rms}. In order to make the accurate evaluation, we have selected the numerical cases for larger water depth, Case 1b and 2b, which are relative to the experiment by Komori, et al. [65]. The transformed significant wave height is summarized in Table 5.2.

Table **5.2**: The significant wave height corresponding to the magnitude of the free-surface fluctuation.

	The magnitude of the free-surface fluctuation : η_{rms}	The significant wave height: Hs (=1.6η_{rms})
Case 1b (Re=150, Water depth: δ)	0.20mm	0.32mm
Case 2b (Re=300, Water depth: δ)	0.25mm	0.40mm

Studies on the growth of wind waves were undertaken by many investigators since Sverdrup and Munk [75] by means of significant waves representing wind-wave field. The results have been practically used for the prediction of wind waves. Wilson [76] proposed empirical formulae for wind waves in the growth stage from many observation results, such as

$$H^*_{10} = 0.30\left[1-\left\{1+0.004(X)^{1/2}\right\}^{-2}\right], \tag{5.2}$$

and

$$T^*_{10} = 1.37\left[1-\left\{1+0.008X^{1/3}\right\}^{-5}\right], \tag{5.3}$$

where $H^*_{10} \equiv gH_s / U_{10}{}^2$, $T^*_{10} \equiv gT_s / 2\pi U_{10}$ and $X \equiv gF / U_{10}{}^2$; H_s, T_s, and F are the wave height, the period of significant waves, the fetch, respectively. The acceleration of gravity g and the wind speed at 10m level U_{10} are employed. This relation improves the fetch graph of Sverdrup and Munk [75]. Mitsuyasu, et al. [77] proposed the following formulas, being based on the data obtained in the wave-tank experiments and the field observations in Hakata Bay:

$$H^*_{10} = 2.15\times10^{-3} X^{0.504}, \tag{5.4}$$

and

$$T^*_{10} = 5.07\times10^{-2} X^{0.330}, \tag{5.5}$$

The formulas by Wilson [76] and Mitsuyasu, et al. [77] support the three-second power law [78, 79], which has also been substantiated by data from the wind-wave tunnel experiments and the field observations.

The universal relation between the dimensionless significant wave height H^* and period T^*, that is, as the three-second power law, was derived by Toba [78, 79], being based on the concept that transfer processes of momentum and mechanical energy from the air to the sea are determined locally. This concept suggests that the growth of wind waves is predicted by the fetch and duration. Consequently, F^* and t^* become variables only for the semi-empirical formulations and $u_*{}^*$ is introduced as the parameter for incorporating the mean external condition.

The three-second power law proposed by Toba [78, 79] is derived as follows. For the wind stress acting on wind waves, τ, and the average velocity of horizontal transport of surface water particles u_0 due to the orbital motion of wind waves, the rate of work done by the wind stress to wind waves, is given by τu_0. In Stokes' wave, that is an irrotational wave of finite amplitude, u_0 is given by

$$u_0 = \kappa^2 a^2 C, \tag{5.6}$$

to the second order of the wave amplitude a,where κ means the wave number expressed by

$$\kappa = \frac{2\pi}{L} = \frac{\sigma^2 g}{L} = \frac{g}{C^2}. \tag{5.7}$$

Here, L is the wave length, and σ is the peak angular frequency of wind waves. The phase velocity C is related to the period, T, by

$$C = \frac{gT}{2\pi}. \tag{5.8}$$

If a^2 is replaced with the mean square amplitude $\overline{a^2}$, Eq. (5.6) is reduced to

$$u_0 = \frac{\pi^3 H^2}{gT^3} \tag{5.9}$$

according to the relation given by Longuet-Higgins [80]

$$\overline{a^2} = \frac{H^2}{(2.83)^2} = \frac{H^2}{8}. \tag{5.10}$$

Consequently, it follows that

$$\pi u_0 = \frac{u_*{}^* H^{*2}}{T^{*3}} \pi^3 \rho g \nu, \tag{5.11}$$

where $u_*{}^* \equiv u_*^3 / g\nu$, $H^* \equiv gH / u_*^2$, $T^* \equiv gT / u_*$, and $\tau = \rho u_*^2$. A dimensionless quantity that represents the rate of acquisition of wave energy may be written as

$$\frac{u_*{}^* H^{*2}}{T^{*3}}. \tag{5.12}$$

A further hypothesis is introduced as follows. The rate of work done by the wind stress to wind waves, namely, the time rate of increase of the average wave energy per unit horizontal area, depends only on $u_*{}^*$. In the simplest case, it is proportional to $u_*{}^*$ such that

$$\frac{u_*{}^* H^{*2}}{T^{*3}} = B^2 u_*{}^*, \tag{5.13}$$

where B is an universal constant. The following relation is, thus, immediately obtained from Eq. (5.13), that is,

$$H^* = BT^{*3/2}. \tag{5.14}$$

Equation (5.14) is called the three-second power law for wind waves of simple spectrum. The value of B was empirically given as $B = 0.062$ by use of his wind-wave tunnel data and empirical formulas by Wilson [76] and Mitsuyasu, et al. [77]. This is well substantiated by various wind-wave tunnel experiments.

We have examined the three-second power law and the spectrum form of wind waves in the present numerical simulation. In Fig. 5.14, the solid line shows the dimensionless significant wave height H^* given by Eq. (5.14) with the constant $B = 0.062$. Solid triangles and diamonds show the wind-wave tunnel data from Toba [78] and Kawai et al. [81], respectively. Solid circles show the

present numerical results for Case 1b and Case 2b. Figure 5.14 includes almost full range of H^* and T^* for wind waves in the growth stage. The present numerical results are consistent to the three-second power law for relatively young wind waves.

In the usually measured range of the drag coefficient C_D for U_{10} of 0-15m/s, the B-value of 0.062 may vary 10% as reviewed by Blanc [3]. After Blanc [3], by various C_D–formulas, possible range of the B is extended to 0.062±20%. Figure 5.15 shows the same data as used in Fig. 5.14 but in dimensional expressions. These data points are distributed around 0.062. The data points obtained from the present simulations are consistent to the line of $B = 0.062$. Also, it is confirmed that the relation between the period and the height of significant waves is consistent to the three-second power law within error levels coming from the wind-wave tunnel experiment and the field observation.

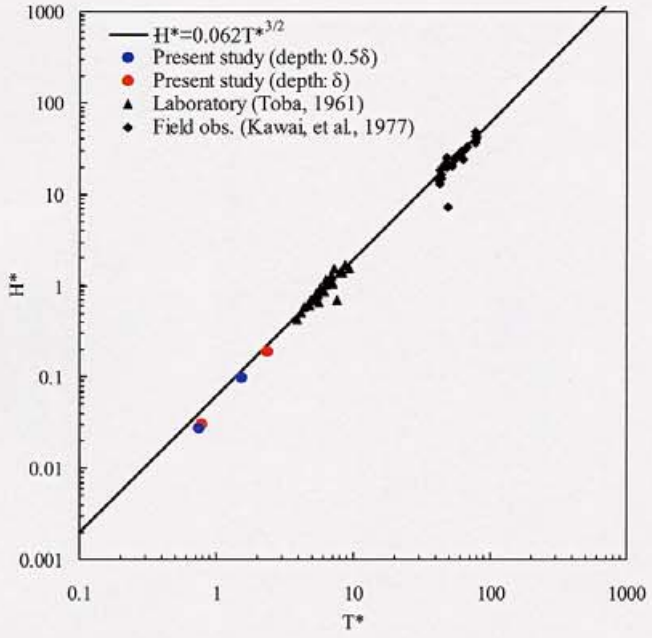

Figure **5.14**: The three-second power law between the nondimensional significant wave height and wave period.

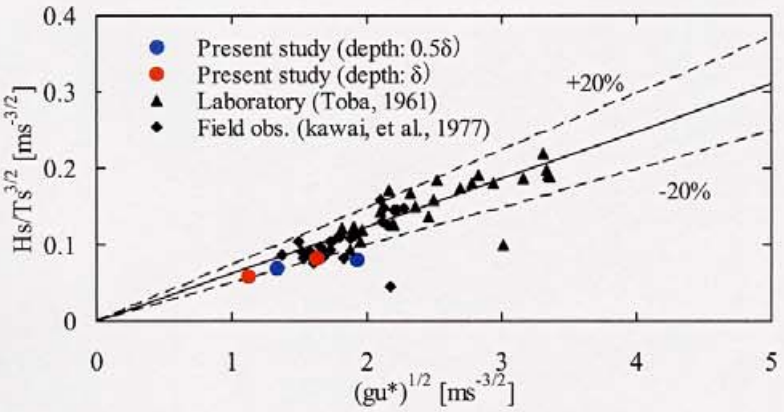

Figure **5.15**: The three-second power law between the significant wave height and wave period.

It is well known that the energy spectrum of growing wind waves has a conspicuous peak, and that the spectral form on the high-frequency side of the maximum is expressed by a negative power law. From a dimensional analysis, Phillips [82] conjectured the existence of an equilibrium range expressed by

$$\phi(\sigma) = \alpha_p g^2 \sigma^{-5}, \tag{5.15}$$

where α_p is a constant. From various observational data, however, it turns out that α_p is not a constant but depends on other factors, such as u_*, which was neglected in the Phillips' analysis.

On the other hand, Toba [83] combined the three-second power law shown in Eq. (5.14) with the concept of similarity of the wind-wave spectra as explained below. Frequency in the spectral peak, σ_p, may be approximately substituted for the significant wave period T with the relation,

$$\sigma_p = \frac{2\pi}{T}. \tag{5.16}$$

The significant wave height H is related to ϕ with

$$\int_0^\infty \phi d\sigma = \frac{\overline{a^2}}{2} = \frac{H^2}{2(2.83)^2} = \frac{H^2}{16}. \tag{5.17}$$

Equation (5.13) is also written in a dimensional form as

$$H^2 = B^2 g u_* T^3. \tag{5.18}$$

The concept of similarity of the wind-wave spectra is summarized such that, if the spectral density ϕ and the angular frequency σ are normalized by its peak value ϕ_p and the spectral peak frequency σ_p, respectively, the spectrum has a unique form in the gravity wave range. Being based on this concept, the following derivation may be possible. For the normalized spectrum and the frequency,

$$\frac{\phi}{\phi_p} = \phi' \tag{5.19}$$

and

$$\frac{\sigma}{\sigma_p} = \sigma' \tag{5.20}$$

it is demanded that

$$\int_0^\infty \phi' d\sigma' = \frac{1}{\phi_p \sigma_p} \int_0^\infty \phi d\sigma = const. = A. \tag{5.21}$$

From Eqs. (5.21) and (5.17), it follows that

$$H^2 = 16 A \phi_p \sigma_p. \tag{5.22}$$

From Eqs. (5.18) and (5.22), together with Eq. (5.16), the form of ϕ_p is given by

$$\phi_p = \alpha_p g u_* \sigma_p^{-4}, \quad \alpha_p = \frac{\pi^3 B^2}{2A}. \tag{5.23}$$

Since the theoretical form of the spectrum is unknown, A is an indeterminate coefficient. Empirically, it was expressed by

$$\phi = \alpha_p g u_* \sigma^{-4}, \tag{5.24}$$

$$\alpha_p = \frac{\pi^3 B^2}{6} = 0.020 \tag{5.25}$$

from wind-wave tunnel data [83]. Kawai, et al. [81] derived the value of α_p from their field observation data using the least-square method, that is,

$$\alpha_p = 0.062 \pm 0.010. \tag{5.26}$$

In Fig. 5.16, the solid line and the broken line show the Eq. (5.24) obtained by the wind-wave tunnel experimental data by Toba [83] with $\alpha_p = 0.020$ and by the field observational data by Kawai, et al. [81] with $\alpha_p = 0.062$, respectively. The red line shows the wind wave spectrum obtained by the present simulations. It is seen that the wind wave spectra resulted from the present simulations are in good agreement with the scaling in Eq. (5.25). Moreover, the amplitudes of the spectra show a better agreement with the data of the wind-wave tunnel experiment than that of the field observation. The result suggests that the present numerical simulation can accurately represent the developing phase of wind waves in wind-wave tunnel experiments.

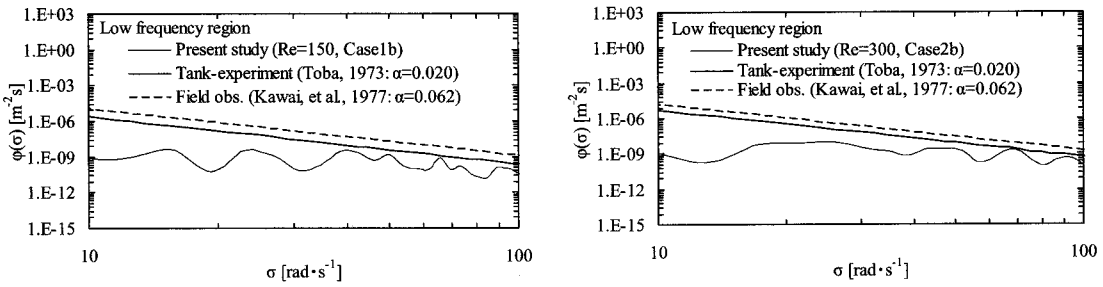

(a) (b)

Figure **5.16**: Wind wave spectral density and the $\alpha g u_* \sigma^{-4}$-form observed by the tank-experiment and the field observation in the gravity wave range.

(a) Case 1b (Re=150, Water depth: δ); (b) Case 2b (Re=300, Water depth: δ)

As the wave number becomes large, the effect of surface tension is becomes dominant. In the range where the surface tension plays a significant role, the gravity acceleration g hitherto used in all equations may be replaced with

$$g_* \equiv g + \frac{S\kappa^2}{\rho_w}, \tag{5.27}$$

from the infinitesimal wave theory. Here, S, κ, and ρ_w denote the surface tension, the wave number, and the density of water, respectively. In the gravity wave range explained in the above, the second term on the right hand side of Eq. (5.27) is neglected. On the other hand, it is assumed that Eq. (5.24) can be expressed in terms of the wave number κ, where

$$\kappa = \frac{\sigma^2}{g}. \tag{5.28}$$

Applying the extension of Eq. (5.27), Eq. (5.24) is rewritten as

$$\phi = \alpha_p g_* u_* \sigma^{-4}. \tag{5.29}$$

Since g_* depends on κ, in order to purely express Eq. (5.29) as a function of σ, one employs

$$\kappa = \frac{\sigma^2}{g_*} = \frac{\sigma^2}{S\kappa^2/\rho_w + g} \tag{5.30}$$

instead of Eq. (5.28). For the capillary wave range, where

$$g << \frac{S\kappa^2}{\rho_w}, \tag{5.31}$$

Eq. (5.29) is reduced to

$$\phi = \alpha_p \left(\frac{S}{\rho_w}\right)^{1/3} u_* \sigma^{-8/3}. \tag{5.32}$$

According to the above result, it is considered that the -4 power line found in the gravity wave range gradually approaches the -8/3 power line for the capillary wave range. In Fig. 5.17, the solid line shows the Eq. (5.32), and the red line shows the wind wave spectrum obtained by the present simulations in the very high frequency region. The wind wave spectrum possesses a good agreement with the $(S/\rho_w)^{1/3} u_* \sigma^{-8/3}$ scaling. The result shows that the present numerical simulation can also resolve accurately the capillary waves with very fine structures.

The present simulations can reproduce the statistical relations, such as the three-second power law and the spectral form for growing wind waves, and are consistent with the wind-wave tunnel experiment and the field observation. The quantitative evaluation of the friction stresses on the free-surface with large shear stress is, therefore, satisfactorily.

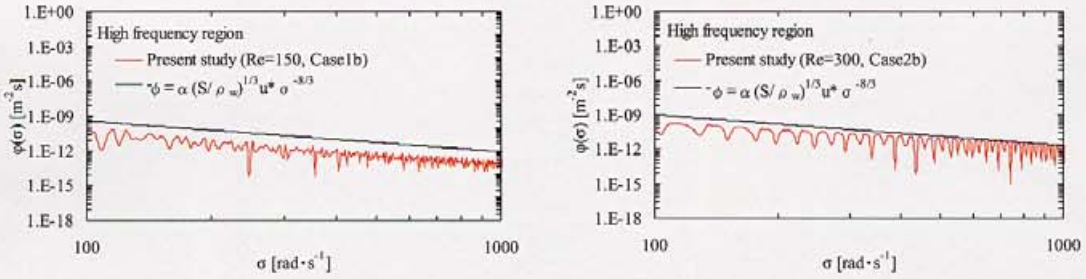

Figure **5.17**: Wind wave spectral density and the $\alpha(S/\rho w)^{1/3} u_* \sigma^{-8/3}$-form in the capillary wave range.
(a) Case 1b (Re=150, Water depth: δ); (b) Case 2b (Re=300, Water depth: δ)

6 Summary

As the first step towards construction of an efficient evaluation method of the momentum transport between Atmosphere and Ocean, which may greatly affect the climate projection, the two-phase flow simulations based on the C-CUP method are carried out. The momentum transport process through a gas-liquid interface under the shear stress is quantitatively investigated in cases that the free-surface deformations can not be ignored. Turbulent Reynolds number Re_τ is changed from 150 to 300 in order to find the wind velocity dependence of the friction. An effect of the water depth on evaluation of the friction velocity is also studied. In the deeper case, the water depth is consistent with that of the tank-experiments. From the statistical analysis of turbulence in the simulation results, we have quantitatively discussed the turbulent structures near the free-surface and the mechanism of the momentum transfer through the gas-liquid interface. The results obtained from the present simulation study on the two-phase flow are summarized below.

It is shown that the vertical velocity fluctuations normal to the free-surface are induced on the liquid side near the interface. To explain this behavior, we have made analysis of the pressure-strain correlation term that remains finite only near the free-surface on the liquid side. The surface-normal component of the pressure-strain correlation term has a positive value while the streamwise component is negative. This behavior indicates that the turbulent energy on the gas side is redistributed mainly into the vertical component of the velocity fluctuations on the liquid side through the free-surface deformations which are excited by the shear stress. Moreover, the result that all vorticity components increase near the free-surface shows the presence of three-dimensional turbulent structures. Thus, it is necessary to take into account the effects of the free-surface deformation on the momentum transfer process through the gas-liquid interface when a large shear stress exists. It is also suggested that the vertical velocity component should be accurately calculated, although the conventional numerical simulations have treated the velocity fields near the free-surface as almost two-dimensional.

The turbulent structures are similar to those of the experiment, in which the representative wind velocity is almost the same as that of the present study. The Reynolds stress distribution seems to be correlated with the free-surface structure. This result means that the momentum transfer through the gas-liquid interface depends on the Reynolds stress produced by the vertical velocity fluctuations near the free-surface. In order to verify the correlation, we have investigated a phase relation between a time series of the Reynolds stress on the gas side and that of the free-surface position. According to this analysis, large positive spikes of the Reynolds stress, which enhance the downward momentum transfer, often appear at positions where the 'burst' and the 'sweep' are observed. It is also consistent with the experiments. In addition, bursts of the Reynolds stress are observed in close to the crest over the windward side, as reported in the experiment. This agreement

suggests that the present simulation captures the bursting phenomena produced by the Reynolds stress in relation to ordered motions such as the wind flow separation and the reattachment over wind waves. Therefore, it is considered that the momentum transfer process with the free-surface deformation can be well reproduced by the present DNS of the two-phase flow.

The friction velocities are evaluated from the peak values of the friction stresses near the free-surface on the liquid side. The relation between the friction velocity and the mean velocity on the gas side is in good agreement with the tank-experimental data for both cases of the Reynolds numbers of 150 and 300. Especially, a better agreement is found for the deeper water condition. In the velocity range considered here, the free-surface deformation can not be ignored in contrast to the conditions for the conventional DNS studies, where the liquid turbulence is decoupled from the gas dynamics by supposing a flat interface and applying the free-slip condition. Therefore, the present study presents the first quantitative evaluation of the friction stresses on the free-surface, which is validated by a comparison with the tank experimental data.

The three-second power law and the spectrum form of wind waves are also examined for the case of the present numerical simulation. The form of the energy spectrum of wind waves is derived from a combination of the three-second power law and the similarity of the spectral form of wind waves. These are well substantiated by data from a wind-wave tunnel experiment. The three-second power law is obtained from the spectrum of wind waves based on the local balance between the wind waves and both the turbulent structures of the air and liquid flows. The period and the wave height of significant waves in dimensionless forms, which are considered to correspond to the peak frequency and the energy level, respectively, are used as representative quantities of wind waves. From the results of the present study, it is confirmed that the relation of the period and the height of significant waves is consistent to the three-second power law within the error coming from the wind-wave tunnel experiment and the field observation. In the gravity wave range, the spectral form on the high frequency side is proportional to the -4 power of the angular frequency of wind waves. The wind waves grow in a way that on the logarithmic diagram of the spectral density versus the angular frequency, the spectrum slides up along the line of the form, keeping its similar form. It is confirmed that the spectral density obtained by the present simulations has the -4 power of the angular frequency. The spectrum level shows a better agreement with the data of the wind-wave tunnel experiment than that of the field observation. The result suggests that the present numerical simulation can accurately represent the developing phase of wind waves in wind-wave tunnel experiments. As the wave number becomes large, the effect of surface tension is incorporated. Thus, the -4 power line found in the gravity wave range gradually approaches the -8/3 power line for the capillary wave range, which is also reproduced by the present simulations.

The obtained results confirm that the present simulation method has a possibility of extension to a larger gas-liquid flow system towards construction of a reliable scheme for evaluating the

friction stress between Atmosphere and Ocean.

References

[1] Bunker, A. F., Charnok, H., and Goldsmith, R. A.: A note on the heat balance of the Mediterranean and Red sea, J. Mar. Res., 40 (1982) 73-84.

[2] Bryden, H. L.: Ocean heat transport, Paper presented at JSC/CCCO meeting on Time series of Ocean measurements, Tokyo, May 11-15 (1981) p21.

[3] Blanc, T. V.: Variation of bulk derived surface flux, stability, and roughness results due to the use of different transfer coefficient schemes, J. Phys. Oceanogr., 15 (1985) 650-669.

[4] Toba, Y. and Koga, M.: A parameter describing overall conditions of wave breaking, whitecapping, sea spray production and wind stress. In *Oceanic Whitecaps*, ed. by E. C. Monahan and G. M. Niocaill, D. Reidel Pub. (1987) 37-47.

[5] Toba, Y., Iida, N., Kawamura, H., Ebuchi, N., and Jones, I. S. F.: Wave dependence of sea-surface wind stress, J. Phys. Oceanogr., 20 (1990) 705-721.

[6] Wu, J.: Wind stress coefficients over sea surface from breeze to hurricane, J. Geophys. Res., 87 (1982) 9704-9706.

[7] Komori, S., Ueda, H., Ogino, F. and Mizushina, T.: Turbulence structure and transport mechanism at the free surface in an open channel flow, Int. J. Heat Mass Transfer, Vol.25, No.4 (1982) 513-521.

[8] Rashidi, M. and Barnerjee, S.: Turbulence structure in free-surface channel flows, Phys. Fluids, Vol.31 (1988) 2491-2503.

[9] Komori, S., Murakami, Y. and Ueda, H.: The relationship between surface-renewal and bursting motions in an open-channel flow, J. Fluid. Mech., Vol.203 (1989) 103-123.

[10] Sarpkaya, T. and Suthon, P.: Interaction of a vortex couple with a free surface, Experiments in Fluids, 11 (1991) 205-217.

[11] Sarpkaya, T.: Brief reviews of some time-dependent flows, J. Fluids Engineering, Vol.114 (1992) 283-298.

[12] Rood, E. P.: Myths, math, and physics of free-surface vorticity, Appl. Mech. Rev., Vol.47. No.6, part2 (1994) S152-S156.

[13] Rashidi, M. and Barnerjee, S.: The effect of boundary conditions and shear rate on streak formation and breakdown in turbulent channel flows, Phys. Fluids A, Vol.2, No.10 (1990) 1827-1838.

[14] Rashidi, M., Hetsroni, G. and Banerjee, S.: Mechanisms of heat and mass transport at gas-liquid interfaces, Int. J. Heat Mass Transfer, Vol.34, No.7 (1991) 1799-1810.

[15] Komori, S., Nagaosa, R. and Murakami, Y.: Turbulence structure and mass transfer across a sheared air-water interface in wind-driven turbulence, J. Fluid. Mech., Vol.249 (1993) 161-183.

[16] Lam, K. and Barnerjee, S.: On the condition of streak formation in a bounded turbulent flow, Phys. Fluids A, Vol.4, No.2 (1992) 306-320.

[17] Handler, R. A., Swean Jr., T. F., Leighton, R. I. and Swearingen, J. D.: Length scales and the energy balance for turbulence near a free surface, AIAA Journal, Vol.31, No.11 (1993) 1998-2007.

[18] Lombardi, P., Angelis, V. D. and Barnerjee, S.: Direct numerical simulation of near-interface turbulence in coupled gas-liquid flow, Phys. Fluids, Vol.8, No.6 (1996) 1643-1665.

[19] Toba, Y.: Similarity laws of wind waves and related problems, Japan Society of Fluid Mechanics, 6 (1987) 103-115.

[20] Unverdi, S. O. and Tryggvasson, G. A.: A front-tracking method for viscous, incompressible, multi-fluids flows, J. Comput. Phys. 100 (1992) 25.

[21] Osher, S. and Sethian, J. A.: Front propagating with curvature-dependent speed: Algorithms based on Hamilton-Jacobi formulations, J. Comput. Phys. 79 (1988) 12.

[22] Peng, D., Merriman, B, Osher, S., Zhao, H. K. and Kang, M: A PDE-based fast local level-set method, J. Comput. Phys. 155 (1999) 410.

[23] Sussman, M., Smereka, P. and Osher, S.: A level set approach for computing solutions to incompressible two-phase flow, J. Comput. Phys. 114 (1994) 146.

[24] Hirt, C. W. and Nichols, B. D.: Volume of fluid (VOF) method for the dynamics of free boundaries, J. Comput. Phys. 39 (1981) 201.

[25] Youngs, D. L.: Time-dependent multi-material flow with large fluid distortion, in *Numerical Methods for Fluid Dynamics*, edited by Morton. K. W. and Baines. M. J. (Academic Press, New York, 1982), p273.

[26] Kothe, D. B., Rider, W. J., Mosso, S. J. and Brock, J. S.: *Volume tracking of interfaces having surface tension in two and three dimensions*, AIAA Paper 96-0859 (1996).

[27] Puckett, E. G., Almgren, A. S., Bell, J. B., Marcus, D. L. and Rider, W. J.: A high-order projection method for tracking fluid interfaces in variable density incompressible flows, J. Comput. Phys. 130 (1997) 269.

[28] Puckett, E. G. and Saltzman, J. S.: A 3D adaptive mesh refinement algorithm for multimaterial gas dynamics, Physica D 60 (1992) 84.

[29] Rider, W. J. and Kothe, D. B.: *Stretching and Tearing Interface Tracking Methods*, AIAA-95-1717, 33rd Aerospace Sciences Meeting and Exibit, Reno, (1995).

[30] Kunugi, T.: Direct numerical algorithm for multiphase flows with free surfaces and interfaces, Proc. ISAC'97 High Performance Computing on Multiphase Flows (1997) 25-30.

[31] Kunugi, T., Satake, S. and Ose, Y.: Direct numerical simulation of turbulent free-surface flow, In Turbulence and Shear Flow Phenomena-1, Edited by S. Banerjee and J. K. Eaton, Begell House Inc. (1999) 621-626.

[32] Kunugi, T., Satake, S. and Ose, Y.: Direct numerical simulation on wave formation and breaking of turbulent free-surface flow, Two-Phase Flow Modelling and Experimentation (1999)

819-826.

[33] Yabe, T. and Xiao, F.: Description of complex and sharp interface during shock wave interaction with liquid drop, J. Phys. Soc. Jpn., 62 (1993) 2537.

[34] Yabe, T. and Xiao, F.: Description of complex and sharp interface with fixed grids in incompressible and compressible fluid, Computer Math. Applic. 29 (1995) 15.

[35] Yabe, T. and Wang, P.: Unified numerical procedure for compressible and incompressible fluid, J. Phys. Soc. Jpn., Vol.60, No.7 (1991) 2105-2108.

[36] Mutsuda, H., Kawai, H., and Yasuda, T.: Numerical Simulation of Two-Phase Flow Using C-CUP Method, Proceedings of Coastal Engineering, JSCE, vol. 45 (1998) 55-59.

[37] Mutsuda, H. and Yasuda, T.: Numerical Simulations for Physical Mechanism of Strongly-Turbulent Air-Water Mixing Layer within Surf Zone, Proceedings of Coastal Engineering, JSCE, vol. 46 (1999) 161-165.

[38] Xiao, F., Yabe, T. and Ito, T.: Constructing an oscillation-preventing scheme for the advection equation by a rational function, Comput. Phys. Commun. 93 (1996) 1.

[39] Xiao, F., Yabe, T., Nizam, G. and Ito, T.: Constructing a multi-dimensional oscillation-preventing scheme for the advection equation by a rational function, Comput. Phys. Commun. 94 (1996) 103.

[40] Yabe, T., Xiao, F., and Utsumi, T.: The constrained interpolation profile method for multiphase analysis, J. Comput. Phys. 169 (2001) 556.

[41] Zalesak, S. T.: Fully multidimensional flux-correlated transport algorithm for fluid, J. Comput. Phys. 31 (1979) 335.

[42] Harlow, F. H. and Welch, J. E.: Numerical calculation of time-dependent viscous incompressible flow with free surface, Phys. Fluid 8 (1965) 2182.

[43] Amsden, A. A. and Harlow, F. H.: A simplified MAC technique for incompressible fluid flow calculations, J. Comput. Phys. 6 (1970) 322.

[44] Patanker, S. V. and Spalding, D. B.: A calculation procedure for heat, mass and momentum transfer in three-dimensional parabolic flows, Int. J. Heat Mass Transfer 15 (1972) 1787.

[45] Patanker, S. V.: Numerical Heat Transfer and Fluid Flows (McGraw-Hill, New York, 1980).

[46] Harlow, F. H. and Amsden, A. A.: Numerical simulation of almost incompressible flow, J. Comput. Phys. 3 (1968) 80.

[47] Issa, R. I.: Solution of the implicitly discretised fluid flow equations by operator-splitting, J. Comput. Phys. 62 (1985) 40.

[48] Zienkiewicz, O. C. and Wu, J.: A general explicit or semi-explicit algorithm for compressible and incompressible flows, Int. J. Num. Meth. Eng. 35 (1992) 457.

[49] Xiao, F. et al.: An efficient model for driven flow and application to a gas circuit breaker, Comput. Model. Sim. Eng. 1 (1996) 235.

References

[50] Bell, J. B. and Marcus, D. L.: A second-order projection method for variable-density floes, J. Comput. Phys. 101, (1992) 334.

[51] Brackbill, J. U., Kothe, D. B. and Zemach, C.: A continuum method for modeling surface tension, J. Comput. Phys., Vol.100 (1992) 335-354.

[52] McAdams, W. H., Woods, W. K. and Heroman Jr., L. C.: Vaporization inside horizontal tubes - Ⅱ benzene-oil mixtures, Trans. ASME, 64 (1942) 193-200.

[53] Landau, L. D. and Lifshiz, E. M.: *Fluid Mechanics* (Pergamon, New York, 1987).

[54] Martin, J. C. and Moyce, W. J.: An experimental study of the collapse of liquid columns on a rigid horizontal plane, Trans. Roy. Soc. London Ser. A, 244 (1952) 312-324.

[55] Koshizuka, S., Oka, Y. and Tamako, H.: A particle method for calculating splashing of incompressible viscous fluid, *Pro. Int. Conf. Mathematics and Computations, Reactor Physics, and Environmental Analysis*, Portland, Oregon, April 30 – May 4, 1995, p. 1514, American Nuclear Society (1995).

[56] Koshizuka, S., Tamako, H. and Oka, Y.: A particle method for incompressible viscous flow with fluid fragmentation, Comput. Fluid Dynamics J., 4 (1995) 29.

[57] Chang, Y. C., Hou, T. Y., Merriman, B., and Osher, S. : A level set formulation of Eulerian interface capturing for incompressible fluid flows, J. Comput. Phys., 124 (1996) 449-464.

[58] Kunugi, T., Satake, S. and Ose, Y.: Direct numerical simulation of carbon-dioxide gas absorption caused by turbulent free surface flow, 3rd Int. Symp. on Turbulence, Heat and Mass Transfer (2000) 225-232.

[59] Iwamoto, Suzuki and Kasagi: DNS Database of Turbulence and Heat Transfer (2002) URL: http://www.thtlab.t.u-tokyo.ac.jp/index-j.html

[60] Yamamoto, Y., Kunugi, T. and Serizawa, A.: Turbulence statistics and scalar transport in an open-channel flow, Journal of Turbulence, 2 (2001) 1-16.

[61] Nagaosa, R. and Saito, T.: Turbulence structure and scalar transfer in stratified free-surface flows, AIChE. J., 43 (1997) 2393-2404.

[62] Handler, R. A., Saylor, J. R., Leighton, R. I. and Rovelstad, A. L.: Transport of a passive scalar at a shear-free boundary in fully developed turbulent open channel flow, Phys. Fluids, Vol.11, No.9 (1999) 2607-2625.

[63] Perot, B. and Moin, P.: Shear free turbulent boundary layers, Part1: physical insights into near-wall turbulence, J. Fluid Mech., 295 (1995) 199-227.

[64] Nagaosa, R. and Saito, T.: On the relationship between the coherent structures and heat and mass transfer mechanism near a free surface in a fully developed turbulence, Trans. Jpn. Soc. Mech. Eng. B, 64, 620 (1998) 57-64.

[65] Komori, S., Nagaosa, R. and Murakami, Y.: Direct numerical simulation of three-dimensional open-channel flow with zero-shear gas-liquid interface, Phys. Fluids A, Vol.5, No.1 (1993)

115-125.

[66] Ebuchi, N., Kawamura, H., and Toba, Y.: Fine structure of laboratory wind-wave surfaces studied using an optical method, Boundary-Layer Meteorology, 39 (1987) 133-151.

[67] Kawamura, H. and Toba, Y.: Ordered motion in the turbulent boundary layer over wind waves, J. Fluid. Mech., 197 (1988) 105-138.

[68] Okuda, K.: Internal flow structure of short wind waves part Ⅱ. The streamline pattern, J. Oceanogr. Soc. Jpn, Vol.38 (1982) 313-322.

[69] Okuda, K.: Internal flow structure of short wind waves part Ⅳ. The generation of flow in excess of the phase speed, J. Oceanogr. Soc. Jpn, Vol.40 (1984) 46-56.

[70] Yoshikawa, I., Kawamura, H., Okuda, K. and Toba, Y.: Turbulent structure in water under laboratory wind waves, J. Oceanogr. Soc. Jpn, Vol.44 (1988) 143-156.

[71] Toba, Y.: Drop production by bursting of air bubbles on the sea surface (Ⅲ). Study by use of a wind flume, Memoirs, Coll. Sci., Univ. Kyoto, Ser. A, 29 (1961) 71-80.

[72] Okuda, K.: Internal flow structure of short wind waves part Ⅰ. On the internal vorticity structure, J. Oceanogr. Soc. Jpn, Vol.38 (1982) 28-42.

[73] Sugihara, Y., Takasaki, A., and Matsunaga, N.: Structure of turbulent boundary layer beneath wind waves, Proceedings of Coastal Engineering, JSCE, Vol.46 (1999) 96-100.

[74] Rashidi, M., Fenech, H. and Banerjee, S.: Turbulence structure near gas-liquid interface, 22nd IAHR Congress, Lausanne, Switzerland (1987).

[75] Sverdrup, H. U. and Munk, W. H.: Wind, sea and swell. Theory of relations for forecasting. U. S. Hydrogr. Office, Wash., Publ. No. 601 (1947) 1-44.

[76] Wilson, B. W.: Numerical prediction of ocean waves in the North Atlantic for December, 1959. Deut. Hydrogr. Z., 18 (1965) 114-130.

[77] Mitsuyasu, H., Nakayama, R., and Komori, T.: Observations of the wind and waves in Hakata Bay. Rep. Res. Inst. Appl. Mech., Kyusyu Univ., 19 (1971) 37-74.

[78] Toba, Y.: Local balance in the air-sea boundary processes, Ⅰ. On the growth process of wind waves. J. Oceanogr. Soc. Jpn, Vol.28 (1972) 109-120.

[79] Toba, Y.: Local balance in the air-sea boundary processes, Ⅱ. Partition of wind stress to waves and current. J. Oceanogr. Soc. Jpn, Vol.29 (1973) 70-75.

[80] Longuet-Higgins, M. S.: On the statistical distribution of the heights of sea waves. J. Mar. Rea., 11 (1952) 245-266.

[81] Kawai, S. Okuda, K., and Toba, Y.: Field data support of three-seconds power law and $gu_*\sigma^{-4}$ -spectral form for growing wind waves. J. Oceanogr. Soc. Jpn, Vol.33 (1977) 137-150.

[82] Phillips, O. M.: The equilibrium range in the spectrum of wind-generated waves. J. Fluid Mech., 4 (1958) 426-434.

[83] Toba, Y.: Local balance in the air-sea boundary processes, Ⅲ. On the spectrum of wind waves.

References

J. Oceanogr. Soc. Jpn, Vol.29 (1973) 209-220.

Acknowledgements

I express deep thanks to Dr. K. Takahashi, the group leader of Multiscale Simulation Research Group of The Earth Simulator Center for supervising of the work and her much contribution to this study, to my colleagues of Multiscale Simulation Research Group of The Earth Simulator Center for their encouragement and valuable comments.

I wish to express special gratitude to Ass. Prof. T. Watanabe of National Institute of Fusion Science for his comments that have improved the paper.

I am grateful to Prof. T. Yabe of Tokyo Institute of Technology for his valuable comments and kindly suggestions, to Ass. Prof. H. Mutsuda of Hiroshima University for his valuable comments and helpful discussions.

I am indebted to Prof. T. Sato, the director-general of The Earth Simulator Center for his stimulating comments and discussion, and also supporting the work. I further acknowledge gratefully Prof. K. Watanabe, the program director of Holistic Simulation Research Program of The Earth Simulator Center for gracious and helpful discussions that greatly improved this study.

The computations contained in the paper were performed by the use of The Earth Simulator at The Earth Simulator Center, Yokohama, Japan.

Finally, I am also thankful to my parents for supporting the living during this study, to Miss M. Takahata for her encouragement and devoted support.